

Hyperon I: Partial wave amplitudes for K^-p scattering

M. Matveev^{1,2}, A.V. Sarantsev^{1,2}, V.A. Nikonov^{1,2}, A.V. Anisovich^{1,2}, U. Thoma¹, and E. Klempt^{1a}

¹Helmholtz–Institut für Strahlen– und Kernphysik, Universität Bonn, 53115 Bonn, Germany

²National Research Centre “Kurchatov Institute”, Petersburg Nuclear Physics Institute, Gatchina, 188300 Russia

July 9, 2019

Abstract. Early data on K^- induced reactions off protons are collected and used in a coupled-channel partial wave analysis (PWA). Data which had been published in the form of Legendre coefficients are included in the PWA. In a *primary* fit using 3^* and 4^* resonances only, we observe some significant discrepancies with the data. In a systematic search for new Λ and Σ hyperon resonances, additional candidates are found. The significance of the known and of the additional resonances is evaluated. Seventeen resonances listed with 1^* or 2^* and one resonance listed with 3^* in the Review of Particle Properties cannot be confirmed, five new hyperons are suggested. The partial-wave amplitudes deduced in this analysis are compared to those from other analyses.

1 Introduction

The spectrum of N^* 's and Δ^* 's is presently studied vigorously in a number of photoproduction experiments at ELSA, JLab, MAMI, and SPring-8 (see Refs. [1, 2]). In the first excitation shell, seven negative-parity resonances (five N^* 's and two Δ^* 's) are expected in the quark model [3]; these are known since long. In the second excitation shell, 21 positive-parity states are predicted [4], 16 of them have been observed, even though only 11 of them are considered to be established (with 3^* 's or 4^* 's in the notation of the Review of Particle Physics, RPP) [5]. But there is the chance that existing or new data with further analyses will add to our knowledge of the missing or not so well-known states.

In the hyperon spectrum, seven negative-parity Λ^* 's and seven negative-parity Σ^* 's resonances are expected in the first excitation shell. SU(3) links the seven Σ^* 's and five Λ^* 's to the spectrum of N^* 's and Δ^* 's. Two further SU(3) singlet Λ^* 's are expected. Compared to this expectation, one Λ^* resonance with spin-parity $J^P = 3/2^-$ is missing but only four negative-parity Σ^* 's are established. Only a small fraction of the predicted spectrum of positive-parity hyperon resonances is known. Clearly, our knowledge on the hyperon spectrum needs to be improved.

In this paper we study the possibility to find missing hyperon (Λ^* and Σ^*) resonances in existing data. The paper is motivated by recent advances of coupled-channel partial-wave analyses of the existing data of K^-p reactions [6, 7, 8, 9, 10, 11], and by the prospects of new data on hyperon spectroscopy from J-PARC [12], JLAB [13], and the forthcoming PANDA experiment [14].

The pioneering work of Ref. [6, 7] reported the first coupled-channel partial wave analysis of most available

data on Kaon induced reactions. In a first step [6], the authors constructed the partial-wave amplitudes for the reaction $\bar{K}N \rightarrow \bar{K}N, \pi\Sigma, \pi\Lambda$ in slices of the invariant mass in the range from $W = \sqrt{s} = 1.48$ GeV to 2.1 GeV. In a second step [7], these partial-wave amplitudes were fit using a multichannel parametrization in the form $S = B^T R B = I + 2iT$, where T is the partial-wave T -matrix, R a generalized multichannel Breit-Wigner matrix, and B and its transpose B^T are unitary matrices describing non-resonant background. In these energy-dependent fits, the partial-wave amplitudes of two-body reactions in sliced bins in the invariant mass were exploited as well as the results of partial wave analyses on the reactions $K^-p \rightarrow \pi\Lambda(1520), \pi\Sigma(1385), K^*N$, and $\bar{K}\Delta$.

The partial-wave amplitudes from Ref. [6] were also used by the authors of Ref. [11] exploiting a K -matrix formalism where poles are described as conventional pole terms and background contributions by poles at negative values of s . The energy-dependent amplitudes from their fit described reasonably well the energy-independent partial-wave amplitudes from Ref. [6] even though some significant discrepancies can be seen. When the observables were calculated from the energy-dependent amplitudes [11], severe discrepancies showed up.

Kamano *et al.* [8, 9] fitted a similar set of data on the reactions $\bar{K}N \rightarrow \bar{K}N, \pi\Sigma, \pi\Lambda, \eta\Lambda, K\Xi$ and quasi-two-body final states as reported in [6]. They tried two different models A and B (containing different sets of resonances) and compared their amplitudes with the energy independent amplitudes of [6]. The three sets of amplitudes (from [6] and from models A, B of Ref. [8]), are consistent for the dominant partial waves but show larger discrepancies for smaller partial-wave amplitudes. It is hence not surprising that the spectrum of hyperon resonances obtained in the three analyses [7, 9, 11] agree only in the

^a email: klempt@hiskp.uni-bonn.de

Table 1. List of reactions used in the partial wave analysis. Δ denotes the $\Delta(1232)3/2^+$, Λ^* the $\Lambda(1520)3/2^-$, Σ^* the $\Sigma(1385)3/2^+$.

$K^-p \rightarrow K^-p$	$K^-p \rightarrow \bar{K}^0n$	$K^-p \rightarrow \pi^0\Lambda$
$K^-p \rightarrow \omega\Lambda$	$K^-p \rightarrow \eta\Lambda$	$K^-p \rightarrow \pi^0\Sigma^0, \eta\Sigma^0$
$K^-p \rightarrow \pi^\mp\Sigma^\pm$	$K^-p \rightarrow K^{+/\prime}\Xi^{-/\prime}$	$K^-p \rightarrow K^{-/\prime}\Delta^{+/\prime}$
$K^-p \rightarrow \pi^\pm\Sigma^{*\mp}$	$K^-p \rightarrow \pi^0\Lambda^*$	$K^-p \rightarrow K^{*-}p$
$K^-p \rightarrow K^{*0}n$	$K^-p \rightarrow \pi^0\pi^0\Lambda$	$K^-p \rightarrow \pi^0\pi^0\Sigma$

leading contributions. Technically, it often remains open why one resonance is included in a fit and another one is not.

Already in 2000, the Gießen group [15] applied modern analysis techniques to study the reactions $K^-p \rightarrow \pi\Sigma$ and to $\pi\Lambda$. The authors solved the Bethe-Salpeter equation in an unitary K-matrix approximation and fitted the partial-wave amplitudes derived in [16]. The measurements of total cross sections compiled in [17] were imposed as constraints. Masses, widths and partial decay widths of the leading resonances below 1700 MeV were determined.

New data in the low-mass region stimulated further investigations. A new Crystal Ball collaboration was formed at BNL – exploiting a detector that had originally been built to study the charmonium spectrum [18] and which was then transferred to DESY to study a wide range of particle physics including two-photon collisions [19]. Subsequently, the detector was exploited for hadron spectroscopy at BNL [20] and is presently used at MAMI in Mainz [21] for photoproduction experiments.

At BNL, the Crystal Ball collaboration made significant contributions to the spectroscopy of low-mass hyperons. Several reactions were studied at eight incident K^- momenta between 514 and 750 MeV. Differential and total cross sections and the hyperon polarization were reported for the reaction $K^-p \rightarrow \eta\Lambda$ [22] and $K^-p \rightarrow \pi^0\Lambda$, $K^-p \rightarrow \pi^0\Sigma$, and $K^-p \rightarrow \bar{K}^0n$ [23] (see also [24]), $K^-p \rightarrow \pi^0\pi^0\Lambda$ [25], $K^-p \rightarrow \pi^0\pi^0\Sigma$ [26]. A new path to hyperon spectroscopy was opened in Refs. [27, 28, 29].

This paper is part of a comprehensive study of the hyperon spectrum. In this paper, a fit is presented to (nearly) all available data on K^-p induced reactions. The reactions used in the fit are shown in Table 1. The emphasis of this paper lies on two-body final states and on a determination of the hyperon resonances needed to achieve a good fit to the data. In [30], data on three-body and quasi-two-body final states are discussed. In that paper, we present properties of hyperon resonances in detail and compare the resulting spectrum with the Bonn quark model [31]. In [32], we present a fit of low-energy data on K^- induced reactions, including data on K^-p at rest, and found that only one pole is required to describe the $\Lambda(1405)1/2^-$ region. For the threshold region, data on K^-p properties at rest are also very important: The decay ratios $\Gamma_{K^-p \rightarrow \pi^+\Sigma^-} / \Gamma_{K^-p \rightarrow \pi^-\Sigma^+}$, $\Gamma_{K^-p \rightarrow \pi^0\Lambda} / \Gamma_{K^-p \rightarrow \text{neutral}}$, and $\Gamma_{K^-p \rightarrow \pi^\pm\Sigma^\mp} / \Gamma_{K^-p \rightarrow \text{inelastic}}$ were taken from Refs. [33, 34]. The SIDDHARTA experiment at DAΦNE determined the

energy shift and width of the 1S level of the kaonic hydrogen atom [35, 36]. These data proved to be very important for the study of the $\Lambda(1405)$ region [37, 38, 39, 40, 41, 42, 43, 44, 45, 46, 47, 48] which suggested the existence of two isoscalar poles in the $\Lambda(1405)$ region. In [49] we present a coupled-channel partial wave analysis of CLAS data on $\gamma p \rightarrow K^+(\pi\Sigma)$ [28] and $K^+(\bar{K}N)$ [50] and argue that photoproduction may offer new chances to study hyperon resonances.

The paper is organized as follows: First, in Section 2, a short outline of the BnGa partial-wave-analysis method is presented. In Section 3, we list the data used in this analysis. The search for new or less established resonances is described in Section 4. The results of the final fit are presented in Section 5. In Section 6, we suggest a possible star rating for the resonances used in the final fit. Our partial wave amplitudes for $\bar{K}N \rightarrow \bar{K}N$ and $\bar{K}N \rightarrow \pi\Sigma$ scattering in isospin $I = 0$ and $I = 1$ and for $\bar{K}N \rightarrow \pi^0\Lambda$ scattering are compared to those from other analyses in Section 7. The paper concludes in Section 8 with a short summary.

2 The BnGa partial wave analysis

2.1 The scattering amplitude

The general form of the amplitude for meson-baryon scattering can be written as

$$A(s, t) = \sum_{IJJN} C_I Q_{JJN}(s, t) A_{IJJN}(s), \quad (1)$$

where $IJJN$ are isospin, total spin and ‘‘naturalness’’. C_I are the Clebsch-Gordan coefficients which depend on the isospin of all particles in the process (including intermediate states). $A_{IJJN}(s)$ are partial wave amplitudes, and the $Q_{JJN}(s, t)$ tensors describe the angular dependent part of the partial wave amplitudes. The naturalness is an alternative way to describe the parity; it is given by $N = (-1)^{(n+1)}P$ where n corresponds to the rank of the partial wave, $J = n + 1/2$. The angular dependent part is constructed from the decay vertices, polarization vectors and tensors which describe the structure of the particle propagators (see [51]). For example, the angular part for the scattering of a pseudoscalar meson and a $J^P = 1/2^+$ baryon is given by

$$Q_{J\pm}(s, t) = \bar{u}(q_1) \tilde{N}_{\alpha_1 \dots \alpha_n}^{(\pm)}(q^\perp) F_{\xi_1 \dots \xi_n}^{\alpha_1 \dots \alpha_n}(P) \times N_{\xi_1 \dots \xi_n}^{(\pm)}(k^\perp) u(k_1). \quad (2)$$

Here, the k_1 and q_1 are the momenta of the initial and final-state baryons, and k_2 and q_2 are the momenta of the initial and final-state mesons; the relation $P = (k_1 + k_2) = (q_1 + q_2)$, $s = P^2$ holds true. The momenta k^\perp and q^\perp are relative momenta in the initial and final states orthogonal to the total momentum P :

$$k_\mu^\perp = \frac{1}{2}(k_1 - k_2)_\nu g_{\mu\nu}^\perp, \quad q_\mu^\perp = \frac{1}{2}(q_1 - q_2)_\nu g_{\mu\nu}^\perp, \\ g_{\mu\nu}^\perp = g_{\mu\nu} - \frac{P_\mu P_\nu}{P^2}. \quad (3)$$

The baryons are described with bispinors:

$$\begin{aligned} u(p) &= \frac{1}{\sqrt{2m(p_0+m)}} \begin{pmatrix} (p_0+m)\omega \\ (\mathbf{p}\sigma)\omega \end{pmatrix}, \\ \bar{u}(p) &= \frac{1}{\sqrt{2m(p_0+m)}} \begin{pmatrix} \omega^*(p_0+m) \\ -\omega^*(\mathbf{p}\sigma) \end{pmatrix}. \end{aligned} \quad (4)$$

Here, ω represents a 2-dimensional spinor and ω^* the conjugated and transposed spinor, and we use the normalization condition

$$\bar{u}(p)u(p) = 1, \quad \sum_{\text{polarizations}} u(p)\bar{u}(p) = \frac{m + \hat{p}}{2m}. \quad (5)$$

The structure of the resonance propagator corresponds to a convolution of the polarization vectors of the resonances and have the following covariant form:

$$F_{\nu_1 \dots \nu_n}^{\mu_1 \dots \mu_n} = (-1)^n \frac{\sqrt{s+\hat{P}}}{2\sqrt{s}} O_{\xi_1 \dots \xi_n}^{\mu_1 \dots \mu_n} T_{\beta_1 \dots \beta_n}^{\xi_1 \dots \xi_n} O_{\nu_1 \dots \nu_n}^{\beta_1 \dots \beta_n}, \quad (6)$$

where

$$\begin{aligned} T_{\beta_1 \dots \beta_n}^{\xi_1 \dots \xi_n} &= \frac{n+1}{2n+1} (g_{\xi_1 \beta_1} - \frac{n}{n+1} \sigma_{\xi_1 \beta_1}) \prod_{i=2}^n g_{\xi_i \beta_i}, \\ \sigma_{\alpha_i \alpha_j} &= \frac{1}{2} (\gamma_{\alpha_i} \gamma_{\alpha_j} - \gamma_{\alpha_j} \gamma_{\alpha_i}). \end{aligned} \quad (7)$$

The $O_{\nu_1 \dots \nu_n}^{\mu_1 \dots \mu_n}$ describe the structure of the boson propagator for the particle with spin $J = n$ and are constructed from the metrical tensors orthogonal to the momentum of the resonance, see Eqn. (3). For the lowest spin states,

$$\begin{aligned} O = 1, \quad O_{\nu}^{\mu} &= g_{\mu\nu}^{\perp} = g_{\mu\nu} - \frac{P_{\mu} P_{\nu}}{s}, \\ O_{\nu_1 \nu_2}^{\mu_1 \mu_2} &= \frac{1}{2} \left(g_{\mu_1 \nu_1}^{\perp} g_{\mu_2 \nu_2}^{\perp} + g_{\mu_1 \nu_2}^{\perp} g_{\mu_2 \nu_1}^{\perp} - \frac{2}{3} g_{\mu_1 \mu_2}^{\perp} g_{\nu_1 \nu_2}^{\perp} \right). \end{aligned} \quad (8)$$

For higher states, the operator can be calculated using the recurrent expression

$$\begin{aligned} O_{\nu_1 \dots \nu_L}^{\mu_1 \dots \mu_L} &= \frac{1}{L^2} \left(\sum_{i,j=1}^L g_{\mu_i \nu_j}^{\perp} O_{\nu_1 \dots \nu_{j-1} \nu_{j+1} \dots \nu_L}^{\mu_1 \dots \mu_{i-1} \mu_{i+1} \dots \mu_L} - \right. \\ &\quad \frac{4}{(2L-1)(2L-3)} \times \\ &\quad \left. \sum_{\substack{i < j \\ k < m}}^L g_{\mu_i \mu_j}^{\perp} g_{\nu_k \nu_m}^{\perp} O_{\nu_1 \dots \nu_{k-1} \nu_{k+1} \dots \nu_{m-1} \nu_{m+1} \dots \nu_L}^{\mu_1 \dots \mu_{i-1} \mu_{i+1} \dots \mu_{j-1} \mu_{j+1} \dots \mu_L} \right). \end{aligned} \quad (9)$$

The operator $O_{\nu_1 \dots \nu_n}^{\mu_1 \dots \mu_n}$ provides the symmetry and traceless condition for the indices within one group and the orthogonality to the particle momentum. The structure of the $T_{\nu_1 \dots \nu_n}^{\mu_1 \dots \mu_n}$ operator is unique and is defined by the orthogonality condition to the γ -matrix and the normalization condition

$$F_{\nu_1 \dots \nu_n}^{\mu_1 \dots \mu_n} F_{\xi_1 \dots \xi_n}^{\nu_1 \dots \nu_n} = (-1)^n F_{\xi_1 \dots \xi_n}^{\mu_1 \dots \mu_n}. \quad (10)$$

The vertex functions $N_{\alpha_1 \dots \alpha_n}^{(\pm)}$ describe the spin structure of a resonance decaying into a baryon with $J^P = 1/2^+$ and a pseudoscalar meson. The decay orbital momentum is connected with the total spin as $J = L + \frac{1}{2}$ for the '+' states and as $J = L - \frac{1}{2}$ for the '-' naturality states.

$$\begin{aligned} N_{\mu_1 \dots \mu_n}^{(+)}(k^{\perp}) &= X_{\mu_1 \dots \mu_n}^{(n)}(k^{\perp}) \quad L = n, \\ N_{\mu_1 \dots \mu_n}^{(-)}(k^{\perp}) &= i\gamma_5 \gamma_{\nu} X_{\nu \mu_1 \dots \mu_n}^{(n+1)}(k^{\perp}) \quad L = n + 1, \end{aligned} \quad (11)$$

where $X_{\mu_1 \dots \mu_n}^{(n)}(k^{\perp})$ is the orbital momentum operator which depends on the relative momentum orthogonal to the momentum of the decaying particle:

$$\begin{aligned} X^{(0)} &= 1, \quad X_{\mu}^{(1)} = k_{\mu}^{\perp} = \frac{1}{2} (k_1 - k_2)_{\nu} g_{\mu\nu}^{\perp}, \\ X_{\mu_1 \mu_2}^{(2)} &= \frac{3}{2} \left(k_{\mu_1}^{\perp} k_{\mu_2}^{\perp} - \frac{1}{3} k_{\perp}^2 g_{\mu_1 \mu_2}^{\perp} \right), \\ X_{\mu_1 \mu_2 \mu_3}^{(3)} &= \frac{5}{2} \left[k_{\mu_1}^{\perp} k_{\mu_2}^{\perp} k_{\mu_3}^{\perp} - \frac{k_{\perp}^2}{5} (g_{\mu_1 \mu_2}^{\perp} k_{\mu_3}^{\perp} + g_{\mu_1 \mu_3}^{\perp} k_{\mu_2}^{\perp} + g_{\mu_2 \mu_3}^{\perp} k_{\mu_1}^{\perp}) \right]. \end{aligned} \quad (12)$$

The operators $X_{\mu_1 \dots \mu_L}^{(L)}$ for $L \geq 1$ can be written in the form of the recurrence expression

$$X_{\mu_1 \dots \mu_L}^{(L)} = k_{\alpha}^{\perp} Z_{\mu_1 \dots \mu_L}^{\alpha}, \quad (13)$$

where

$$\begin{aligned} Z_{\mu_1 \dots \mu_L}^{\alpha} &= \frac{2L-1}{L^2} \sum_{i=1}^L X_{\mu_1 \dots \mu_{i-1} \mu_{i+1} \dots \mu_L}^{(L-1)} g_{\mu_i \alpha}^{\perp} - \\ &\quad \frac{2}{L^2} \sum_{\substack{i,j=1 \\ i < j}}^L g_{\mu_i \mu_j}^{\perp} X_{\mu_1 \dots \mu_{i-1} \mu_{i+1} \dots \mu_{j-1} \mu_{j+1} \dots \mu_L}^{(L-1)}. \end{aligned} \quad (14)$$

In our calculations we use the γ -matrices in the standard representation

$$\gamma_0 = \begin{pmatrix} 1 & 0 \\ 0 & -1 \end{pmatrix}, \quad \gamma = \begin{pmatrix} 0 & \sigma \\ -\sigma & 0 \end{pmatrix}, \quad \gamma_5 = \begin{pmatrix} 0 & 1 \\ 1 & 0 \end{pmatrix}. \quad (15)$$

In the c.m.s. of the reaction the scattering amplitude (1) can be rewritten as:

$$\begin{aligned} A(s, t) &= \omega^* [G(s, t) + H(s, t) i(\sigma \mathbf{n})] \omega', \\ G(s, t) &= \sum_L [(L+1)F_L^+(s) - LF_L^-(s)] P_L(z), \\ H(s, t) &= \sum_L [F_L^+(s) + F_L^-(s)] P_L'(z), \end{aligned} \quad (16)$$

where ω and ω' are nonrelativistic spinors and \mathbf{n} is a unit vector normal to the decay plane. The F -functions are

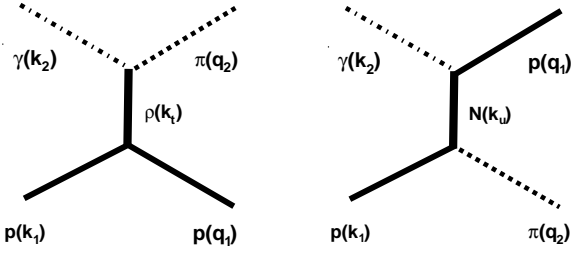


Fig. 1. Diagrams for the t - and u -channel exchange amplitudes.

defined as follows:

$$\begin{aligned}
 F_L^+ &= (|\mathbf{k}||\mathbf{q}|)^L \chi_i \chi_f \frac{\alpha_L}{2L+1} \sum_I A_{I(L+\frac{1}{2})^+}(s), \\
 F_L^- &= (|\mathbf{k}||\mathbf{q}|)^L \chi_i \chi_f \frac{\alpha_L}{L} \sum_I A_{I(L-\frac{1}{2})^-}(s), \\
 \chi_i &= \sqrt{\frac{m_N + k_{N0}}{2m_N}}, \quad \chi_f = \sqrt{\frac{m_N + q_{N0}}{2m_N}}, \\
 \alpha_L &= \frac{(2L-1)!!}{L!}
 \end{aligned} \tag{17}$$

$$\tag{18}$$

The approach through the standard G and H functions is absolutely identical to the our covariant approach, the covariant approach allows us to construct naturally the amplitudes with multibody final states and to perform a combined analysis of all available data sets.

2.2 t and u -channel exchange amplitudes

Non-resonance contributions to the reactions are described by constants in the K -matrix (see below) and by amplitudes for t and u -channel exchanges (see Fig. 1).

The Reggeized amplitudes for t -channel exchange are given by

$$A(t) = g_1(t)g_2(t) \frac{1 + \xi \exp(-i\pi\alpha(t))}{\sin(\pi\alpha(t))} \left(\frac{\nu}{\nu_0}\right)^{\alpha(t)}. \tag{19}$$

Here $\nu = \frac{1}{2}(s - u)$, $\alpha(t)$ is the intercept of the Regge trajectory, and ξ is its signature. We found a significant contribution only from the exchange by the ρ , ω and K^* vector-meson trajectories and the f_0 , a_0 and K_0^* trajectories of scalar mesons.

The u -channel amplitudes are described as the exchange of the corresponding baryon. We observe significant contributions only from exchange of nucleons in the $Kp \rightarrow \Lambda\pi$ and $Kp \rightarrow \Sigma\pi$ reactions. This exchange is represented by a spin-1/2 propagator

$$1/(m_p - \hat{k}_u) \quad \text{where} \quad u = k_u^2. \tag{20}$$

2.3 The structure of the partial wave amplitudes

As the first step we parameterized the partial wave amplitudes as a sum of Breit-Wigner resonances:

$$A(s) = \sum_{\beta} \frac{g_{in}^{\beta} g_{out}^{\beta}}{M_{\beta}^2 - s - iM_{\beta}\Gamma_{tot}^{\beta}} \tag{21}$$

The total width of a resonance is equal to the sum of its partial widths:

$$M_{\beta}\Gamma_{tot}^{\beta} = \sum_j M_{\beta}\Gamma_j^{\beta} = \sum_j \rho_j^{n\pm}(s)(g_j^{\beta})^2, \tag{22}$$

where $J = n + \frac{1}{2}$; $\rho_j^{n\pm}(s)$ is the imaginary part of the loop diagram with vertices given in Eq. (11). In the case of the pseudoscalar meson-baryon channel these functions are given by

$$\begin{aligned}
 \rho_j^{n+}(s) &= \frac{\alpha_n}{2n+1} \frac{|\mathbf{k}_j|^{2n}}{B(n, |\mathbf{k}_j|^2, R)} \frac{m+k_0}{2m} \frac{2|\mathbf{k}_j|}{16\pi\sqrt{s}}, \\
 \rho_j^{n-}(s) &= \frac{\alpha_{n+1}}{n+1} \frac{|\mathbf{k}_j|^{2n+2}}{B(n+1, |\mathbf{k}_j|^2, R)} \frac{m+k_0}{2m} \frac{2|\mathbf{k}_j|}{16\pi\sqrt{s}},
 \end{aligned} \tag{23}$$

where $k_j = (k_0, \mathbf{k})$ is momentum of the final-state baryon in the channel j calculated in the resonance rest system. The Blatt-Weiskopf form factor $B(n, |\mathbf{k}_j|^2, R)$ (with $R = 0.8$ fm) is introduced to provide the correct asymptotic behavior of the phase volume at large energies.

The phase volumes for the three particle final states are described by the spectral integral which has all corresponding cuts and branching points in the complex plane of the total energy. The formulae for these functions are given in [52].

In the case of overlapping resonances the sum of Breit-Wigner amplitudes can violate the unitarity condition. In this case one can use the K -matrix approach which satisfies unitarity. Here the partial wave amplitudes are represented by a matrix with elements which describe the transition between channels i and j ($i, j = pK, \pi\Lambda, \pi\Sigma \dots$) in the form

$$A_{ij}(s) = K_{im}(I - i\hat{\rho}\hat{K})_{mj}^{-1}, \tag{24}$$

where $\hat{\rho}$ is the diagonal matrix of the phase volumes. The K -matrix is parameterized as a sum of K -matrix poles and nonresonant contributions,

$$K_{ij} = \sum_{\beta} \frac{g_i^{\beta} g_j^{\beta}}{M_{\beta}^2 - s} + f_{ij}. \tag{25}$$

This parameterization does not take into account rescattering effects described, e.g., by triangle diagrams. For baryons this effects exists even for two-particle final states since the pseudoscalar meson can be re-absorbed by the baryon. To take into account such effects, we substitute the K -matrix approach by the so-called D -matrix approach [53]. Here the amplitude has the form:

$$A_{ij}(s) = K_{im}(I - i\hat{\rho}\hat{K})_{mk}^{-1}(i\hat{\rho}\hat{D})_{kj} + D_{ij}, \tag{26}$$

where the D -matrix is given by

$$D_{ij} = \sum_{\beta} \frac{g_i^{\beta} G_j^{\beta}}{M_{\beta}^2 - s} + F_{ij}. \tag{27}$$

Table 2. Differential cross sections for $K^-p \rightarrow K^-p$ elastic and $K^-p \rightarrow \bar{K}^0n$ charge exchange scattering used in this analysis. Listed are the reaction, the momenta at which the data are given with a reference, the number of data points, and the χ^2 from the primary (χ_1^2) and from the final fit (χ_2^2).

Reaction	Mass	Ref.	N_{data}	χ_1^2	χ_2^2	
$K^-p \rightarrow K^-p$	1464 1466 1469 1472 1475 1478 1481 1484 1488 1491 1494 1498 1501 1505 1509 1512 1516 1520 1524 1528 1532 1536 1540 1544 1548	[54]	482	1313	990	
	1732 1749 1758 1763 1768 1772 1777 1789	[55]	320	760	694	
	1775 1796 1815 1833 1852 1870 1889 1907 1925 1941 1957	[56]	451	1216	852	
	1858 1869 1877 1887 1902 1911 1921 1930	[57]	311	406	408	
	2207 2246 2288 2328 2365 2397 2436	[58]	75	189	124	
	1696 1687 1681 1671 1662 1652 1642 1633 1624 1615 1606 1595 1586 1578 1569 1561 1552 1544 1536	[59]	752	1054	827	
	1611 1626 1640 1654 1667 1680 1692 1704 1715 1726 1735 1746 1757 1767	[60]	491	810	675	
	1689 1702 1717 1724 1734 1744 1748 1754 1763 1772 1779 1789 1804 1814 1822 1831 1841 1848 1856 1865 1875 1879 1898	[61]	896	969	907	
	1735 1763 1798 1810 1819 1876 1909 1946	[62]	219	306	259	
	1970 1992 2014 2037 2059 2080 2102 2123 2144 2186 2207 2227 2248 2268 2288	[63]	327	833	656	
	1785 1832 1860 1892 1924 2122	[64]	162	465	431	
	2122 2137 2151 2166 2181 2196 2212 2229 2244 2260 2276 2292 2331 2348 2365 2382 2400 2417	[65]	268	1202	811	
	1837 1849 1859 1869 1879 1889 1854 1911 1922 1933 1944 1956 1967	[66]	416	1868	1687	
	$K^-p \rightarrow \bar{K}^0n$	1466 1469 1472 1475 1478 1481 1484 1488	[54]	64	383	182
		1491 1494 1498 1501 1505 1509 1512 1516 1520 1524 1528 1532 1536 1540 1544	[54]	297	696	475
		1732 1749 1758 1763 1768 1772 1777 1789	[55]	160	276	267
1775 1796 1815 1833 1852 1870 1889 1907 1925 1941 1957		[56]	220	744	558	
1858 1869 1877 1887 1902 1911 1921 1930 1935 1949 1963 1976 1992		[57]	260	414	387	
2207 2246 2288 2328 2365 2397 2436		[58]	75	177	102	
1696 1687 1681 1671 1662 1652 1642 1633 1624 1615 1606 1595 1586 1578 1569 1561 1552 1544 1536		[59]	380	618	572	
1569 1589 1598 1620 1634 1647 1659 1676		[23]	128	325	216	
1729 1739 1741 1747 1755 1763 1775 1780 1794		[67]	333	400	398	
1915 1939 1963 1984 2006 2027 2042 2068 2088 2111 2125 2151 2169		[68]	260	515	394	
1569 1578 1587 1597 1606 1615 1624 1633 1643 1652 1661 1670 1680 1689 1708 1717 1726 1736 1745 1755 1763 1773		[69]	808	1837	1237	
1689 1702 1717 1724 1734 1744 1748 1754 1763 1772 1779 1789 1804 1814 1822 1831 1841 1848 1856 1865 1875 1879 1898		[70]	460	498	534	

In the present analysis we describe the decay parameters of the D-matrix by

$$G_j^\beta = g_j^\beta \exp(i\phi_j^\beta), \quad \text{and} \quad F_{ij} = f_{ij} \exp(i\phi_{ij}). \quad (28)$$

The (small) phases take into account the contribution of multiparticle scattering diagrams.

3 The data and the *primary* fit

A detailed survey of the data that are used here in a coupled-channel analysis is presented in Tables 2 to 5. The tables list the reactions, the invariant masses at which measurements have been performed, and the references to the data. N_{data} gives the total number of data points for a reaction. In the last line of Table 2, e.g., there are differential cross sections at 20 angles and for 23 momenta giving $N_{\text{data}}=460$. The χ^2 for these data achieved in the *primary* fit (using only established hyperons and a relativistic Breit-Wigner description of the contributing resonances) and in the final fit are given in the last two columns.

Some data are slightly incompatible with other data in the normalization. The following scaling factors were applied in the fits:

$$\begin{aligned} K^-p: \quad & d\sigma/d\Omega \quad 1.04 \text{ [64]} \quad 1.10 \text{ [65,66]} \\ & P \quad 0.95 \text{ [62]} \\ \bar{K}^0n: \quad & d\sigma/d\Omega \quad 1.025 \text{ [23]} \\ \pi^- \Sigma^+: \quad & d\sigma/d\Omega \quad 1.03 \text{ [57]} \quad 0.95 \text{ [76]} \\ \pi^0 \Sigma^0: \quad & d\sigma/d\Omega \quad 1.06 \text{ [23]} \end{aligned}$$

Polarization data are important for partial wave analyses but often limited in statistics. Also other low-statistics data like $K^-p \rightarrow K\Xi$ can be described rather badly without significantly affecting the total χ_{tot}^2 . To avoid this, data are given a weight. The differential cross section for the final states $\eta\Lambda$, $\omega\Lambda$, and $K\Xi$ get a weight of 3, the corresponding polarization data a weight of 6. Also the data on the quasi-two-body reactions get a weight: 2 for K^*p ; 3 for $\bar{K}\Delta(1232)$; 10 for $\pi\Lambda(1520)$. The polarization data for the $\pi\Lambda$ final state get a weight factor 2, those for $\pi\Sigma$ of 4. The weights are chosen to get a reasonable fit to

Table 3. Differential cross sections on K^-p scattering into two-body final states used in this analysis. Listed are the reaction, the momenta at which the data are given with a reference, the number of data points, and the χ^2 from the primary (χ_1^2) and from the final fit (χ_2^2). (LC: data given as Legendre coefficients).

$K^-p \rightarrow \pi^0 \Lambda$	1732 1749 1758 1763 1768 1772 1777 1789	[55]	160	467	362	
	1775 1796 1815 1833 1852 1870 1889 1907 1925 1941 1957	[56]	220	468	362	
	1858 1869 1877 1887 1902 1911 1921 1930 1935 1949 1963 1976 1992	[57]	256	656	621	
	1696 1687 1681 1671 1662 1652 1642 1633 1624 1615 1606 1595 1586 1578 1569 1561 1552 1544 1536	[59]	380	743	610	
	1569 1589 1598 1620 1634 1647 1659 1676	[23]	125	331	166	
	1729 1739 1741 1747 1755 1763 1775 1780 1794	[67]	341	488	427	
	1689 1702 1717 1724 1734 1744 1748 1754 1763 1772 1779 1789 1804 1814 1822 1831 1841 1848 1856 1865 1875 1879 1898	[70]	460	756	701	
	1915 1939 1963 1984 2006 2027 2042 2068 2088 2111 2125 2151 2169	[71]	260	842	351	
	1648 1657 1666 1675 1684 1692 1702 1711 1719 1728 1737 1746 1754 1763	[72]	126	230	235	
	1600 1630 1648 1663 1678 1693 1708 1722 1740	[73]	90	158	133	
	2207 2246 2288 2328	[74]	60	152	141	
	$K^-p \rightarrow \pi^0 \Sigma^0$	1696 1687 1681 1671 1662 1652 1642 1633 1624 1615 1606 1595 1586 1578 1569 1561 1552 1544 1536	[59]	190	338	383
1569 1589 1598 1620 1634 1647 1659 1676		[23]	125	361	281	
1648 1657 1666 1675 1684 1692 1702 1711 1719 1728 1737 1746 1754 1763		[72]	140	235	229	
1605 1640 1660 1680 1700 1730		[73]	54	88	77	
1569 1589 1598 1620 1634 1647 1659 1676		[24]	72	238	169	
$K^-p \rightarrow \pi^- \Sigma^+$	1732 1749 1758 1763 1768 1772 1777 1789	[55]	160	460	298	
	1775 1796 1815 1833 1852 1870 1889 1907	[56]	220	490	400	
	1858 1869 1877 1887 1902 1911 1921 1930 1935 1949 1963 1976 1992	[57]	259	2838	2224	
	1696 1687 1681 1671 1662 1652 1642 1633 1624 1615 1606 1595 1586 1578 1569 1561 1552 1544 1536	[59]	380	551	439	
	1729 1739 1741 1747 1755 1763 1775 1780 1794	[67]	304	446	400	
	1689 1702 1717 1724 1734 1744 1748 1754 1763 1772 1779 1789 1804 1814 1822 1831 1841 1848 1856 1865 1875 1879 1898	[70]	460	784	627	
	1915 1939 1963 1984 2005 2028 2042 2068 2088 2111 2126 2151 2169	[75]	252	866	577	
	2207 2246 2288 2328 2365 2397 2436	[76]	60	250	276	
	1732 1749 1758 1763 1768 1772 1777 1789	[55]	160	271	205	
	1775 1796 1815 1833 1852 1870 1889 1907 1925 1941 1957	[56]	220	684	381	
$K^-p \rightarrow \pi^+ \Sigma^-$	1858 1869 1877 1887 1902 1911 1921 1930 1935 1949 1963 1976 1992	[57]	259	383	234	
	1696 1687 1681 1671 1662 1652 1642 1633 1624 1615 1606 1595 1586 1578 1569 1561 1552 1544 1536	[59]	380	863	889	
	1729 1739 1741 1747 1755 1763 1775 1780 1794	[67]	306	395	342	
	1689 1702 1717 1724 1734 1744 1748 1754 1763 1772 1779 1789 1804 1814 1822 1831 1841 1848 1856 1865 1875 1879 1898	[70]	460	666	597	
	1915 1939 1963 1984 2005 2028 2042 2068 2088 2111 2126 2151 2169	[75]	240	740	421	
	2207 2246 2288 2328 2365 2397 2436	[76]	57	173	210	
	1664 1665 1666 1667 1668 1669 1670 1672 1674 1676 1678 1680 1682 1683 1685	[22]	135	316	190	
	1664 1671 1681 1687 1696	[59]	25	125	50	
	$K^-p \rightarrow \eta \Lambda$	1750 1765 1780 1795	[77]	16	12	11
	$K^-p \rightarrow K^0 \Xi^0$	2020	[78]	17	15	14
1970 2070 2140		[79]	26	24	15	
2110 2280 2470		[80]	16	20	20	
2150		[81]	8	24	22	
1263 1316 1368 1415 1462 1514 1546 1606 1653 1705 1741 1800 1843 1934 2031 2135 2234 2331		[82]	29	64	46	
1138 1161 1179 1201 1233 1253 1276 1296 1305 1336 1367 1396 1434		[57]				
$K^-p \rightarrow K^+ \Xi^-$	1970 2070 2140	[79]	101	182	168	
	2110 2280 2420 2480	[80]	60	77	66	
	2240	[83]	20	25	18	
	1950	[84]	12	10	10	
	1263 1316 1368 1415 1462 1514 1546 1606 1653 1705 1741 1800 1843 1934 2031 2135 2234 2331 2412 2516	[82]	16	24	16	
	$K^-p \rightarrow \bar{K}^0 n$ (LC)	1709 1738 1758 1767 1782 1803 1821 1846 1865 1887 1919 1937 1953 1970 2001 2022 2051 2085 2106	[86]	136	303	253
$K^-p \rightarrow \pi^0 \Lambda$ (LC)	1709 1738 1758 1767 1782 1803 1821 1846 1865 1887 1919 1937 1953 1970 2001 2022 2051 2085 2106	[86]	128	211	219	
	1647 1656 1673 1677 1692 1698 1709 1715	[87]	40	138	97	

Table 4. Data on the polarization observable P in K^-p scattering used in this analysis. Listed are the reaction, the momenta at which the data are given with a reference, the number of data points, and the χ^2 from the primary (χ_1^2) and from the final fit (χ_2^2).

Reaction	Mass	Ref.	N_{data}	χ_1^2	χ_2^2
$K^-p \rightarrow K^-p$	1630 1652 1669 1687 1706 1720 1811 1827	[88]	134	245	285
	1735 1763 1798 1810 1819 1876 1909 1946	[62]	230	305	275
	1970 1992 2014 2037 2059 2080 2102 2123 2144 2186 2207 2227 2248 2268 2288	[63]	327	801	485
	1785 1832 1860 1892 1924 2122	[64]	168	235	159
	1772 1791 1810 1828 1847 1865 1883 1902 1920	[89]	321	617	455
$K^-p \rightarrow \pi^0\Lambda$	1732 1749 1758 1763 1768 1772 1777 1789	[55]	160	236	162
	1775 1796 1815 1833 1852 1870 1889 1907 1925 1941 1957	[56]	187	371	238
	1569 1589 1598 1620 1634 1647 1659 1676	[23]	123	346	140
	1729 1739 1741 1747 1755 1763 1775 1780 1794	[67]	153	183	155
	1689 1702 1717 1724 1734 1744 1748 1754 1763 1772 1779 1789 1804 1814				
	1822 1831 1841 1848 1856 1865 1875 1879	[70]	160	182	167
	1915 1939 1963 1984 2006 2027 2042 2068 2088 2111 2125 2151 2169	[71]	88	309	210
	2207 2246 2288 2328	[74]	21	69	38
$K^-p \rightarrow \pi^0\Sigma^0$	1569 1589 1598 1620 1634 1647 1659 1676	[23]	124	572	299
$K^-p \rightarrow \pi^-\Sigma^+$	1732 1749 1758 1763 1768 1772 1777 1789	[55]	160	663	672
	1775 1796 1815 1833 1852 1870 1889 1907 1925 1941 1957	[56]	146	236	161
	1729 1739 1741 1747 1755 1763 1775 1780 1794	[67]	92	114	116
	1689 1702 1717 1724 1734 1744 1748 1754 1763 1772 1779 1789 1804 1814				
	1822 1831 1841 1848 1856 1865 1874 1879 1898	[70]	180	236	232
	2207 2246 2288 2328	[76]	15	35	61
$K^-p \rightarrow K^0\Xi^0$	1973 1973 2022 2065 2109 2138 2151 2274 2274 2468	[90]	11	22	19
$K^-p \rightarrow K^-\Xi^+$	1973 1973 2022 2065 2109 2138 2151 2274 2274 2468	[90]	18	17	17

Table 5. Data on the K^-p induced reactions with three-body final states. For all reactions, differential cross sections and three ρ -density matrix elements were expanded into associated Legendre polynomials and Legendre coefficients for $l = 1, \dots, 7$ were determined. Listed are the reaction, the momenta at which the data are given with a reference, the number of data points, and the χ^2 from the primary (χ_1^2) and from the final fit (χ_2^2). Here, Δ denotes $\Delta(1232)3/2^+$, Λ^* is $\Lambda(1520)3/2^-$, and Σ^* denotes $\Sigma(1385)3/2^+$. (LC: data given as Legendre coefficients).

Reaction	Mass	Ref.	N_{data}	χ_1^2	χ_2^2
$K^-p \rightarrow \omega\Lambda$ (LC)	1915 1940 1963 1984 2005 2028 2042 2068 2088 2111 2126 2151 2169	[91]	130	242	147
	1915 1940 1963 1984 2005 2028 2042 2068 2088 2111 2126 2151 2169	[91]	94	314	487
	1988 2012 2031 2051 2070 2088 2105 2120 2136 2151	[92]	100	91	72
	2207 2246 2288 2328 2365 2397 2436	[93]	70	116	89
	1988 2012 2031 2051 2070 2088 2105 2120 2136 2151	[92]	62	173	326
$K^-p \rightarrow 2\pi^0\Lambda$	1571 1589 1598 1620 1632 1650 1659	[25]	26513	$\delta\chi^2 = -244^a$	
$K^-p \rightarrow 2\pi^0\Sigma$	1569 1589 1598 1620 1634 1647 1659 1676	[26]	3286	$\delta\chi^2 = -498^a$	
$K^-p \rightarrow \pi^0\Lambda^*$ (LC)	1919 1942 1964 1986 2006 2027 2042 2068 2088 2111 2126 2151 2168	[94]	377	766	444
	1988 2011 2030 2052 2070 2088 2104 2120 2134 2150	[94]	290	1169	372
$K^-p \rightarrow \pi^0\Lambda^*$ (LC)	1775 1796 1815 1833 1852 1870 1889 1907 1925 1941 1957	[95]	319	606	523
	1710 1728 1747 1759 1775	[95]	25	193	66
$K^-p \rightarrow \pi^-\Sigma^{*+}$ (LC)	1775 1796 1815 1833 1852 1870 1889 1907 1926 1957	[96]	319	547	440
	2005 2028 2042 2068 2088 2110 2126 2151 2167	[96]	135	282	232
$K^-p \rightarrow \pi^+\Sigma^{*-}$ (LC)	1775 1796 1815 1833 1852 1870 1889 1907 1926 1957	[96]	319	524	538
	2005 2028 2042 2068 2088 2110 2126 2151 2167	[96]	126	266	185
$K^-p \rightarrow K^{*-}p$ (LC)	1815 1833 1852 1870 1889 1925 1941 1957	[97]	232	704	636
	1962 1985 2005 2025 2042 2067 2088 2111 2126 2151 2167	[97]	231	323	266
$K^-p \rightarrow K^{*0}n$ (LC)	1815 1833 1852 1870 1889 1907 1925 1941 1957	[97]	261	863	853
	1962 1985 2005 2025 2042 2067 2088 2111 2126 2151 2167	[97]	110	167	129
$K^-p \rightarrow \bar{K}\Delta$ (LC)	1919 1942 1964 1986 2006 2027 2042 2068 2088 2111 2126 2151 2168	[98]	377	547	484
	1988 2011 2030 2052 2070 2088 2104 2120 2134 2150	[98]	290	499	384

^a: From the improvement of the likelihood when primary and final fits are compared.

these data without significantly distorting the fit to the other data sets.

Most data are limited to the region below $W = 2.0$ GeV in the invariant mass; a few data extend the mass region up to $W = 2.4$ GeV. We limit our study to resonances below 2.25 GeV. The data of Tables 2 and 3 include elastic and charge-exchange scattering, the inelastic channels with a Λ hyperon in the final state produced with a π^0 or an η meson, inelastic scattering into the three $\pi\Sigma$ charge states or into $\eta\Sigma$, and the production of cascade hyperons. Table 4 gives references to publications on the polarization observable P . For $K^-p \rightarrow K^-p$ elastic scattering, P was measured by scattering off a polarized target. Hyperons in the final state reveal their polarization P via the asymmetry of their decay.

Table 5 lists the data on $K^-p \rightarrow \Lambda\omega$ and on reactions with three particles in the final state, including quasi-two-body final states. In the low-mass region, we include the data on $K^-p \rightarrow 2\pi^0\Lambda$ [25] and $K^-p \rightarrow 2\pi^0\Sigma$ [26]. For these data, the individual events are available, and we include the data event-by-event in an event-based likelihood fit. We also fit data on the quasi-two-body reactions $K^-p \rightarrow \omega\Lambda$, $K^-p \rightarrow \pi^0\Lambda(1520)$ [94, 95], $K^-p \rightarrow \pi^\mp\Sigma^\pm(1385)$ and $\rho\Lambda$ [96], $\bar{K}N \rightarrow \bar{K}^*N$ [97], and $K^-p \rightarrow \bar{K}\Delta(1232)$ [98]. Details on these reactions are shown in an accompanying paper [30].

We performed four types of fits: one *primary* fit, a series of exploratory fits called *mass scans*, and the *final* fit. At the end, we performed fits in which the significance of the contributing resonances is estimated, and a series of *error defining* fits in which resonances are added in all contributing partial waves.

The *primary* fit to the data listed in Tables 2 to 5 used only those hyperons which were listed in the Review of Particle Properties (RPP) [5] with three or four stars. A list of hyperons used in the *primary* fit and the ranges of masses and widths is given in Table 6. The resonances are mostly well separated and Breit-Wigner parametrisations were used for the resonances. Masses, widths and coupling constants are allowed to vary within the limits quoted in the RPP.

Figure 2 shows the angular distributions expected for $J = 3/2, 5/2$, and $7/2$. They are identical for both parities. Forward-backward asymmetries come from the interference of even and odd waves. This figure can serve as a guide when the data are interpreted.

Figures 3-18 show a comparison of the data with our *primary* (dashed curves) and our *final* (solid curves) fit. Mostly, the two fits show hardly any difference: The established states serve as a rather good approximation. In these figures, no scaling factors are applied, neither to the data nor to the fit.

First, we compare Figs. 3, 4 with Figs. 6, 7. Note that both isospins can contribute to these reactions, with defined Clebsch-Gordan coefficients. Thus, Λ^* and Σ^* resonances both contribute with interfering amplitudes. The K^-p and \bar{K}^0n decay amplitudes of Σ^* resonances have the same, of Λ^* resonances opposite signs: this allows one to separate the Σ^* and Λ^* contributions from the data

Table 6. Hyperons used in the primary fit to the data in which the Breit-Wigner masses and widths from the RPP [5] are imposed.

	J^P	Status	Mass	Width
$\Lambda(1405)$	$1/2^-$	****	$1405_{-1.0}^{+1.3}$	50.5 ± 2
$\Lambda(1670)$	$1/2^-$	****	1660 – 1680	25 – 50
$\Lambda(1800)$	$1/2^-$	***	1720 – 1850	200 – 400
$\Lambda(1520)$	$3/2^-$	****	1519.5 ± 1.0	15.6 ± 1.0
$\Lambda(1690)$	$3/2^-$	****	1685 – 1695	50 – 70
$\Lambda(1830)$	$5/2^-$	****	1810 – 1830	60 – 110
$\Lambda(2100)$	$7/2^-$	****	2090 – 2110	100 – 250
$\Lambda(1600)$	$1/2^+$	***	1560 – 1700	50 – 250
$\Lambda(1810)$	$1/2^+$	***	1750 – 1850	50 – 250
$\Lambda(1890)$	$3/2^+$	****	1850 – 1910	60 – 200
$\Lambda(1820)$	$5/2^+$	****	1815 – 1825	70 – 90
$\Lambda(2110)$	$5/2^+$	***	2090 – 2140	150 – 250
	J^P	Status	Mass	Width
$\Sigma(1750)$	$1/2^-$	***	1730 – 1800	60 – 160
$\Sigma(1670)$	$3/2^-$	****	1665 – 1685	40 – 80
$\Sigma(1940)$	$3/2^-$	***	1900 – 1950	150 – 300
$\Sigma(1775)$	$5/2^-$	****	1770 – 1780	105 – 135
$\Sigma(1660)$	$1/2^+$	***	1630 – 1690	40 – 200
$\Sigma(1385)$	$3/2^+$	****	1382.80 ± 0.35	36.0 ± 0.7
$\Sigma(1915)$	$5/2^+$	****	1900 – 1935	80 – 160
$\Sigma(2030)$	$7/2^+$	****	2025 – 2040	150 – 200

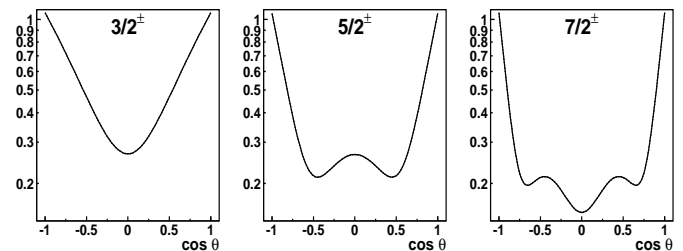


Fig. 2. Shape of angular distributions for K^-p into a Λ^* or Σ^* resonance with given J^P decaying into a $J^P = 1/2^+$ baryon and a pseudoscalar meson. Resonances with $J^P = 1/2^\pm$ yield a flat angular distribution, those with $J^P = 3/2^\pm$: $3 \cos^2 \theta + 1$, $J^P = 5/2^\pm$: $9/4 \cdot (5 \cos^4 \theta - 2 \cos^2 \theta + 1)$, $J^P = 7/2^\pm$: $1/4 \cdot (175 \cos^6 \theta - 165 \cos^4 \theta + 45 \cos^2 \theta + 9)$.

shown in Figs. 3 - 7. Similar arguments hold true for measurements of $K^-p \rightarrow \pi^- \Sigma^+$ and $\pi^+ \Sigma^-$ or $K^+ \Xi^-$ and $K^0 \Xi^0$.

The cross sections for elastic scattering are significantly larger than those for charge exchange. At $W = 1500$ MeV, the former is 2-4 mb/sr while the latter is in the order of 1 mb/sr. At 2000 MeV the elastic cross section rises in

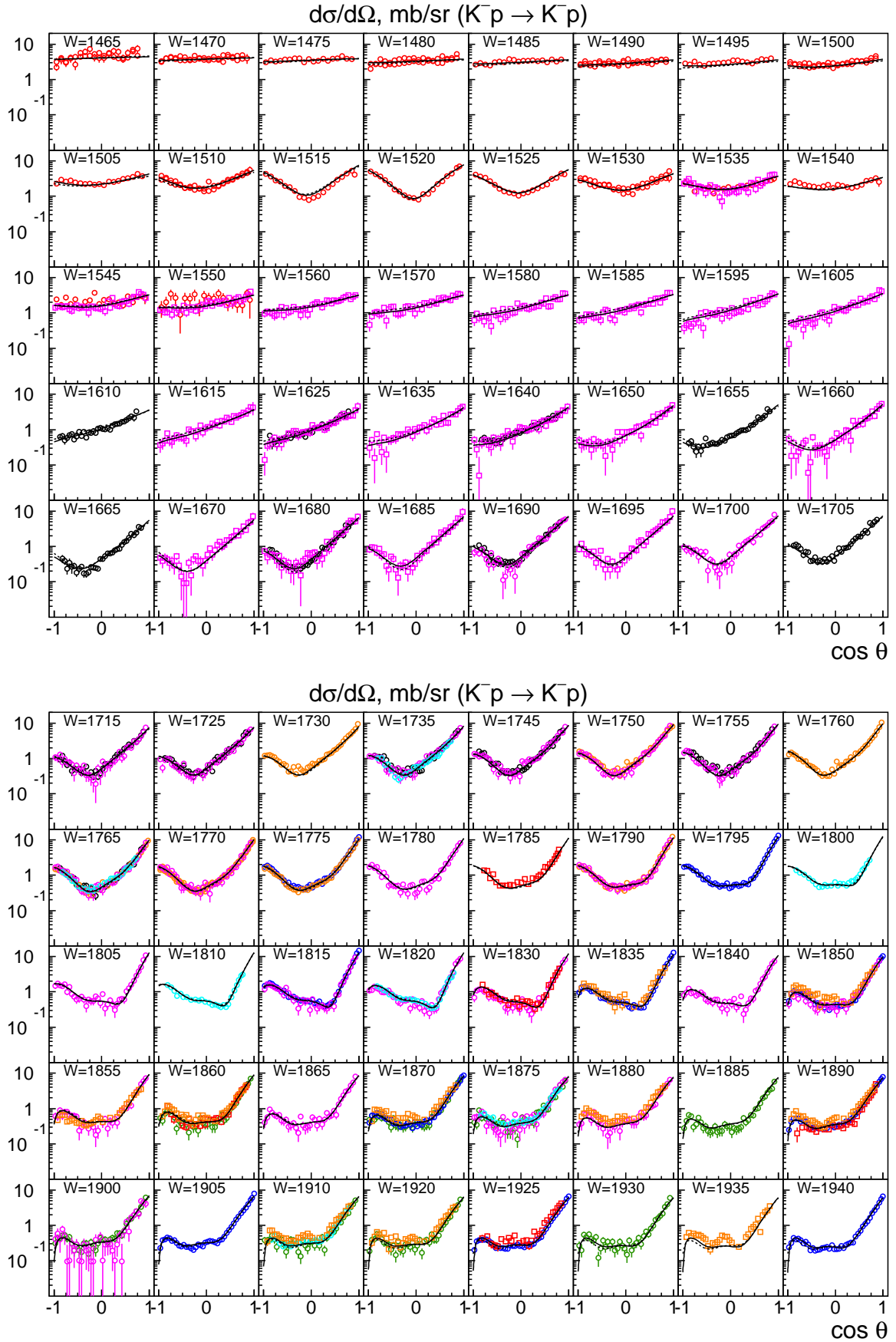


Fig. 3. Differential cross section for the elastic K^-p scattering. The data are from \square [63], \square [64], \square [59], \circ [62], \circ [61], \square [66], \circ [57], \circ [54], \square [65], \circ [56], \square [58], \circ [55]. The solid line represent our final fit.

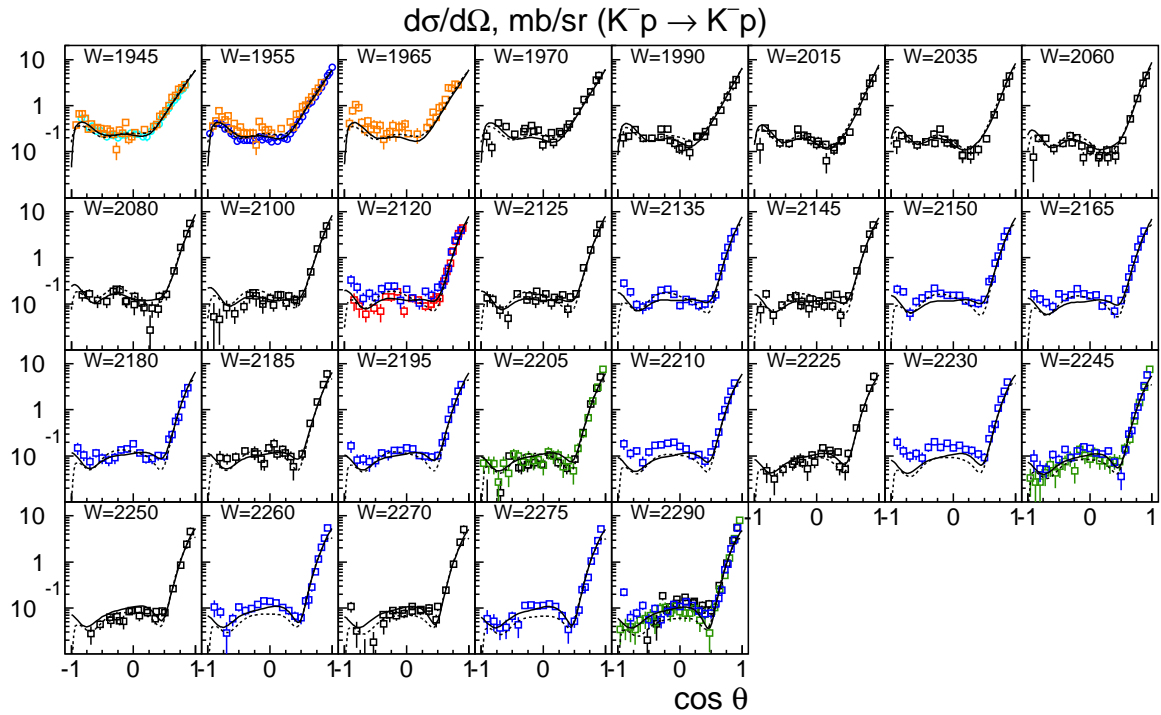


Fig. 4. Differential cross section for the elastic K^-p scattering. See Fig. 3 for the color code.

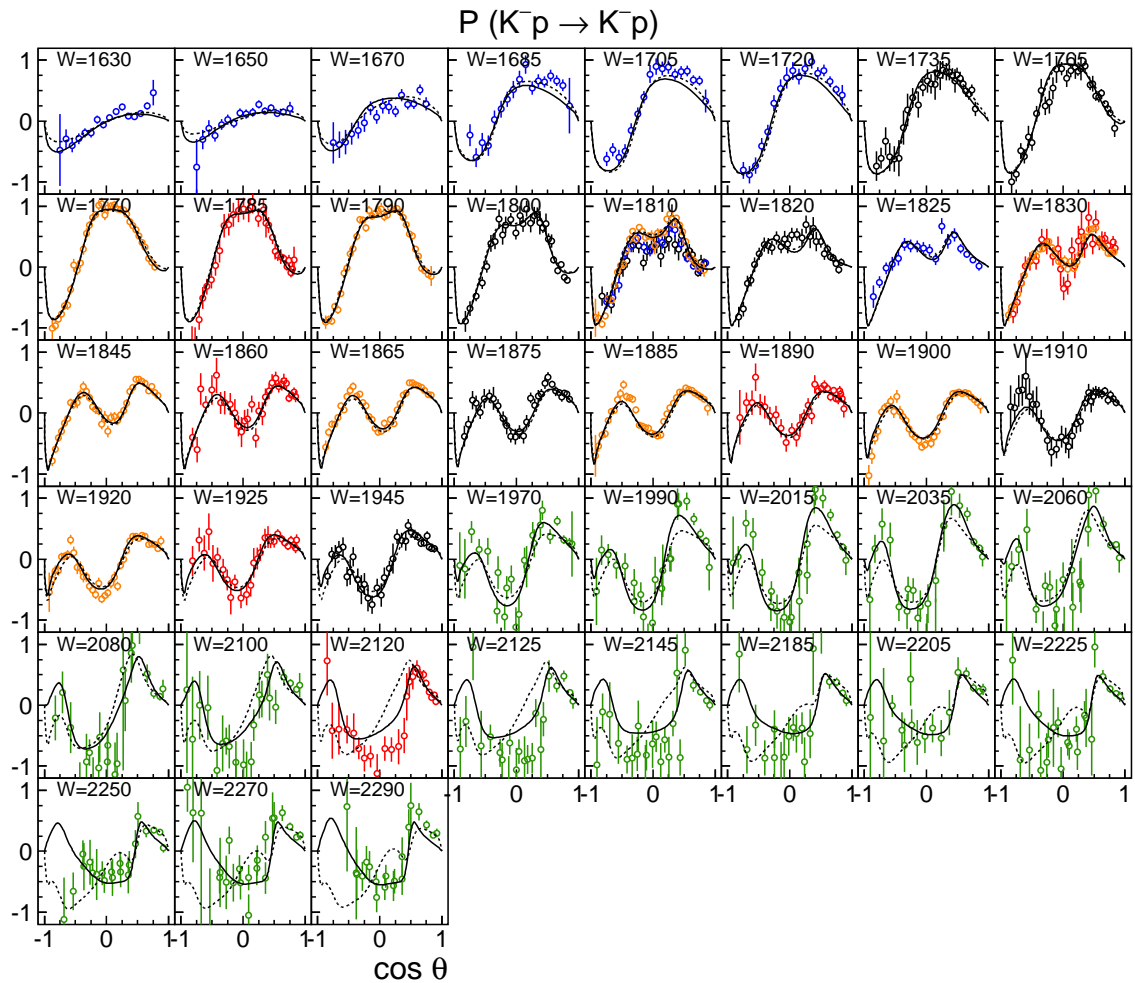


Fig. 5. The polarization observable P for elastic K^-p scattering. The data are from \circ [63], \circ [64], \circ [62], \circ [88], \circ [89].

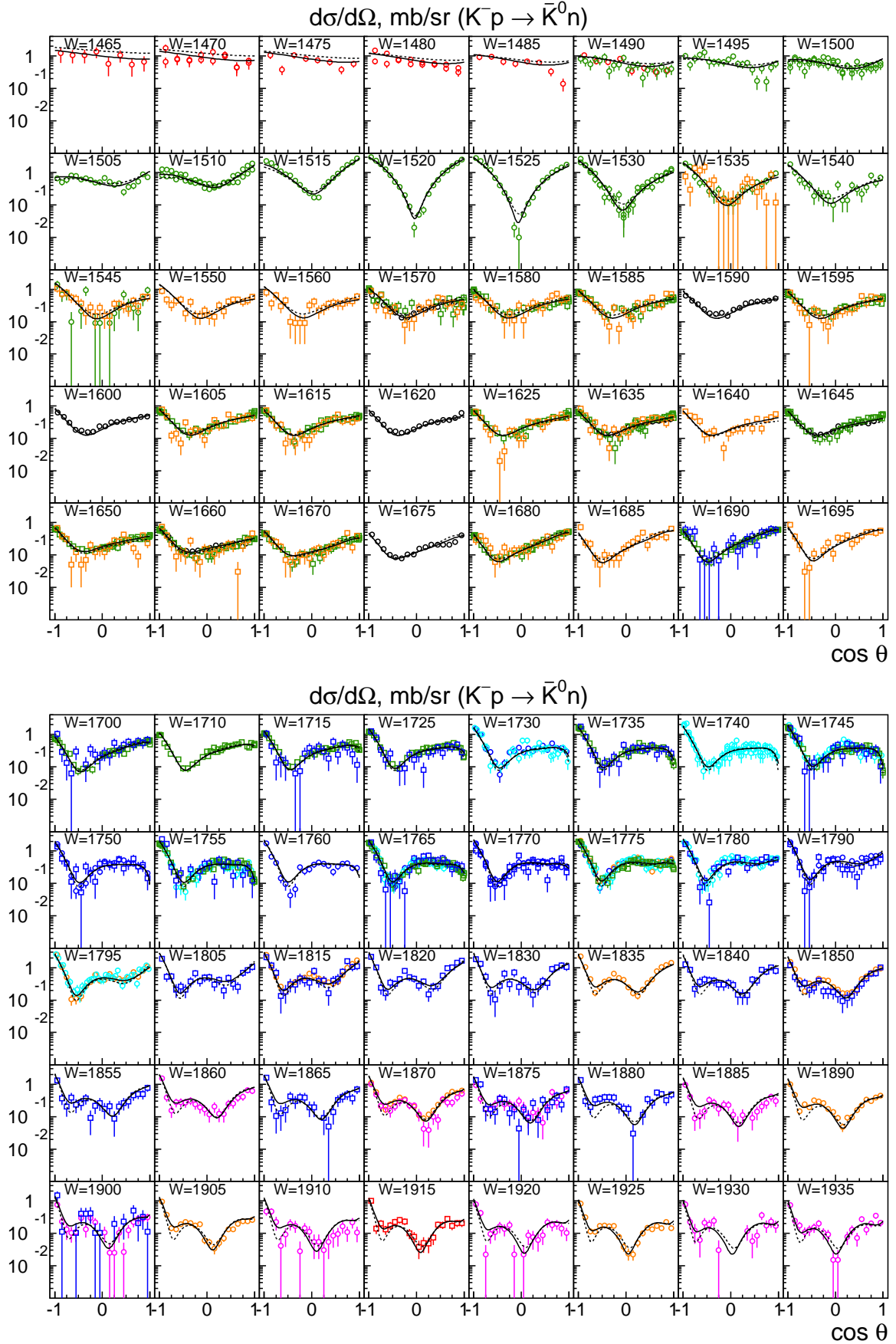


Fig. 6. Differential cross section for the charge-exchange reaction. The data are from \square [59], \square [68], \circ [57], \circ [54]a, \circ [54]b, \circ [56], \square [58], \circ [55], \square [70], \circ [67], \square [69], \circ [23]. The solid line represent our final fit.

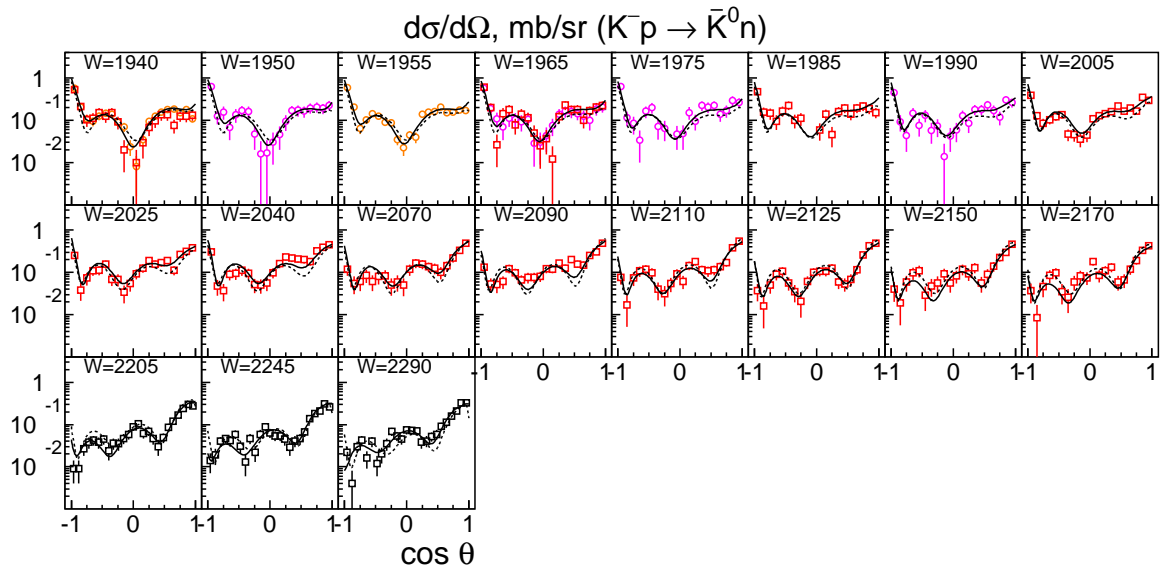


Fig. 7. Differential cross section for the charge-exchange reaction. See Fig. 6 for the color code.

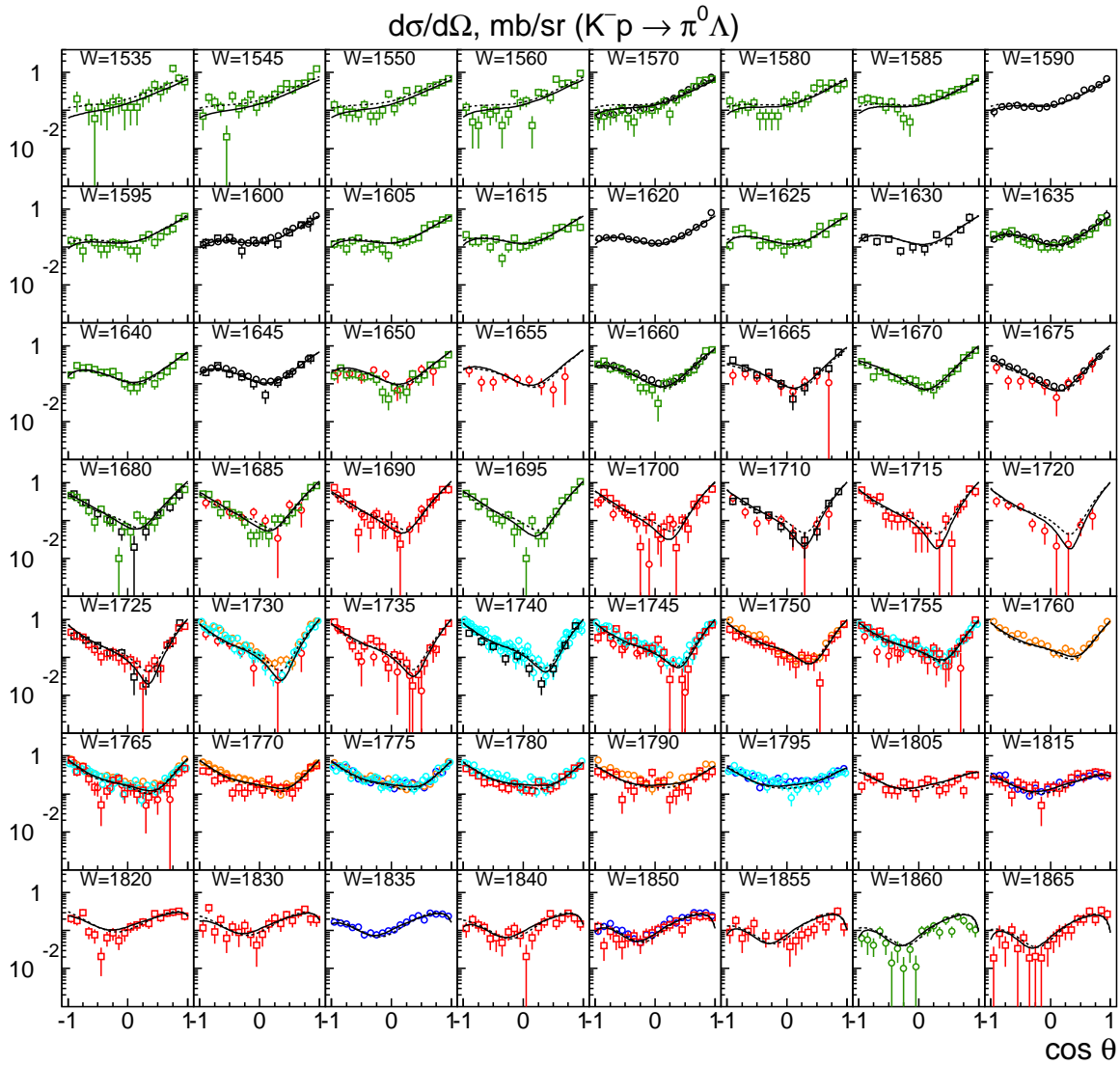


Fig. 8. Differential cross sections for $K^-p \rightarrow \pi^0 \Lambda$. The data are from \square [59], \circ [57], \circ [56], \circ [55], \square [70], \circ [67], \circ [23], \square [71], \circ [72], \square [73], \circ [74].

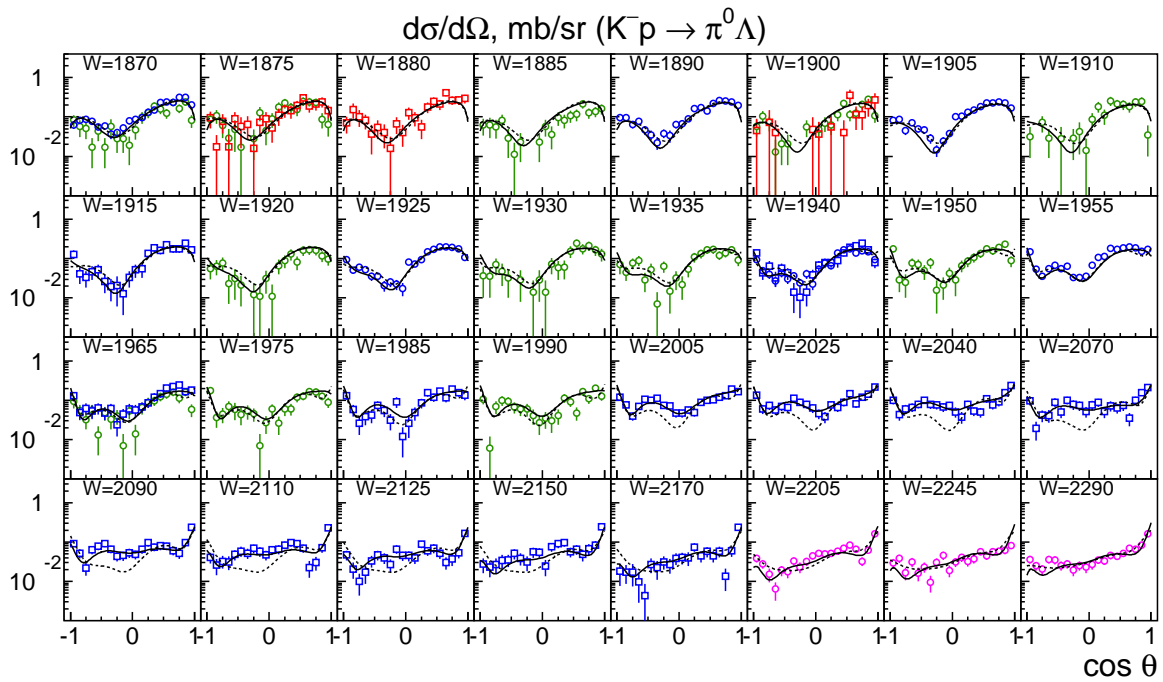


Fig. 9. Differential cross sections for $K^-p \rightarrow \pi^0\Lambda$. See Fig. 8 for the color code.

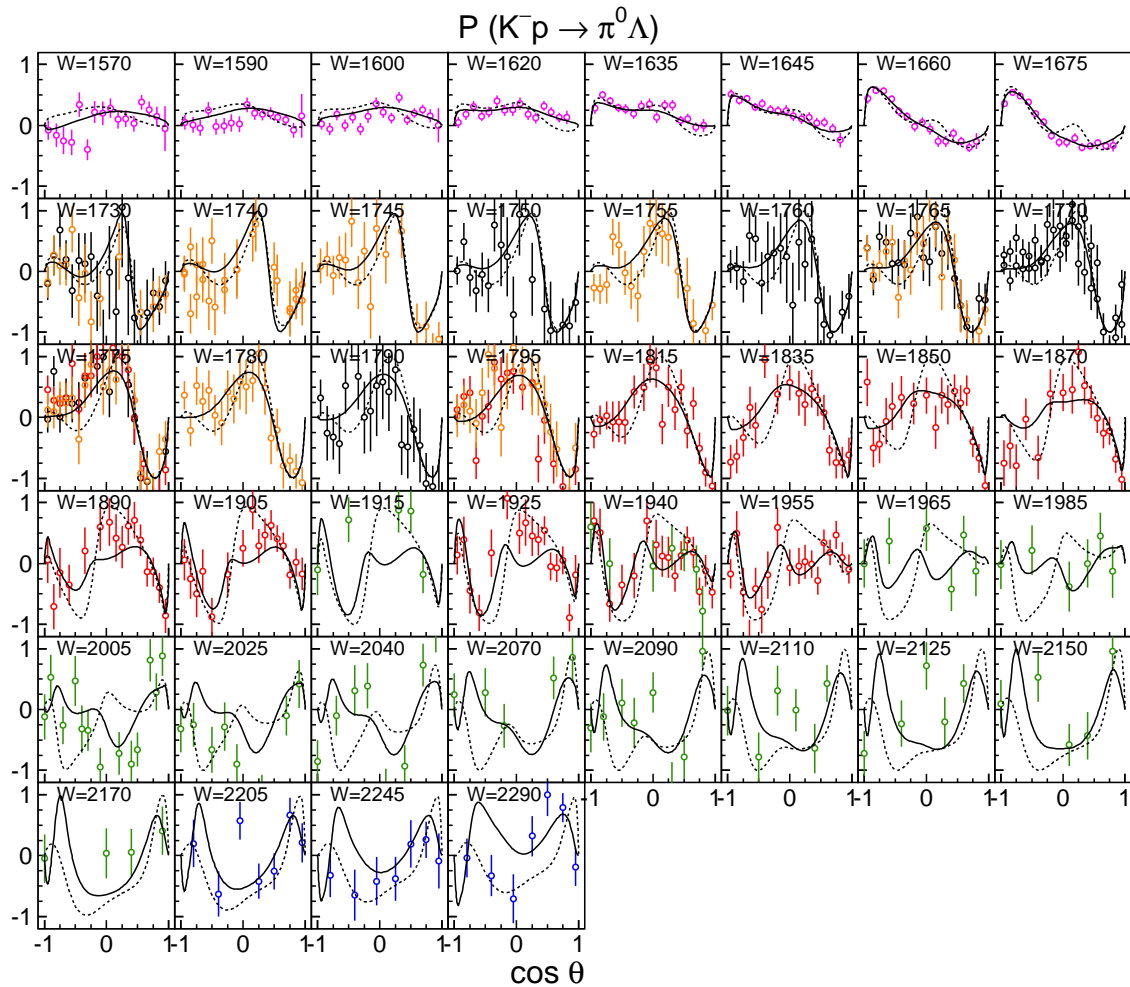


Fig. 10. P for $K^-p \rightarrow \pi^0\Lambda$. The data are from \circ [56], \circ [55], \circ [67], \circ [23], \circ [74].

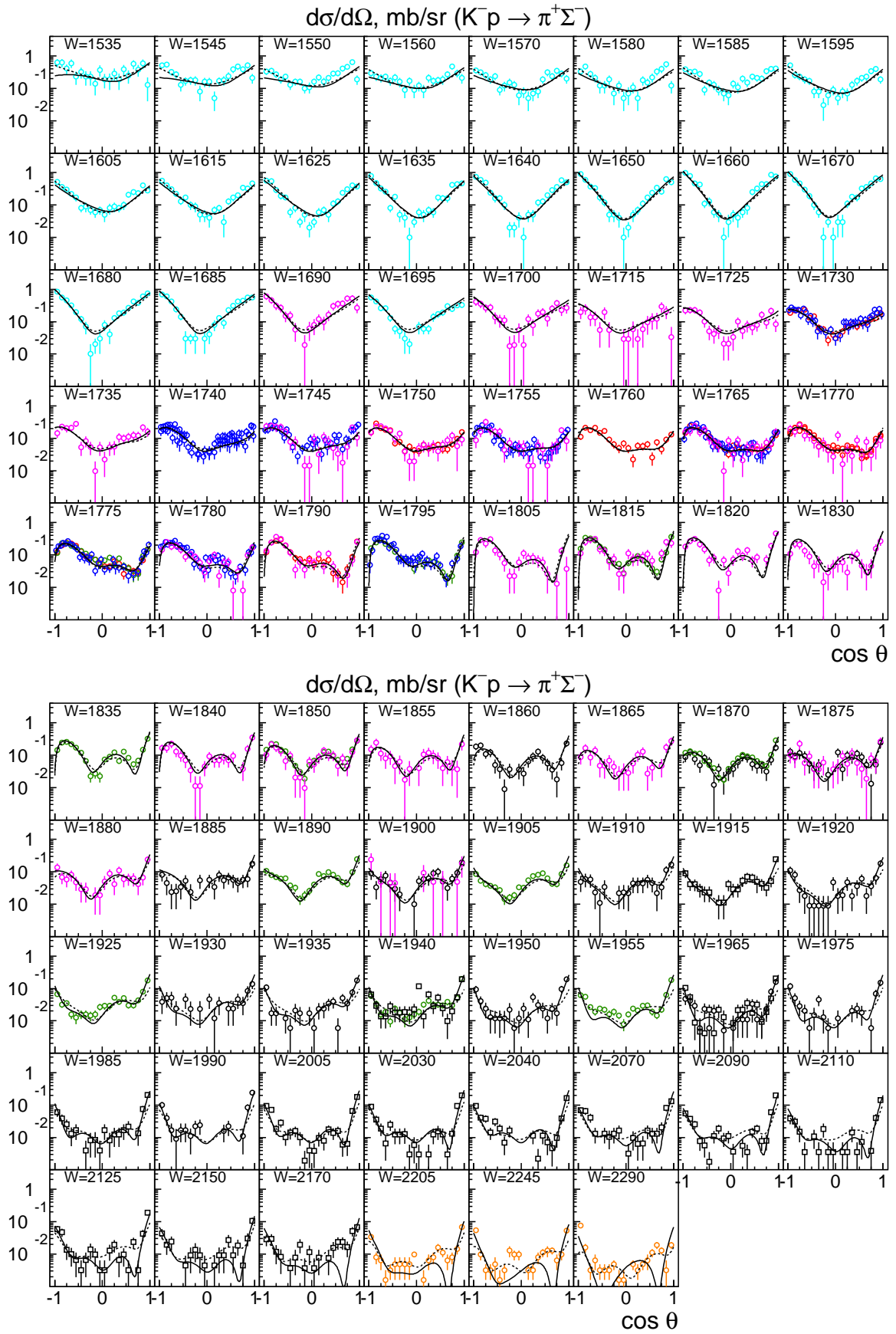


Fig. 11. Differential cross sections for $K^-p \rightarrow \pi^+\Sigma^-$. The data are from \circ [59], \circ [57], \circ [56], \circ [55], \circ [70], \circ [67], \square [75], \circ [76].

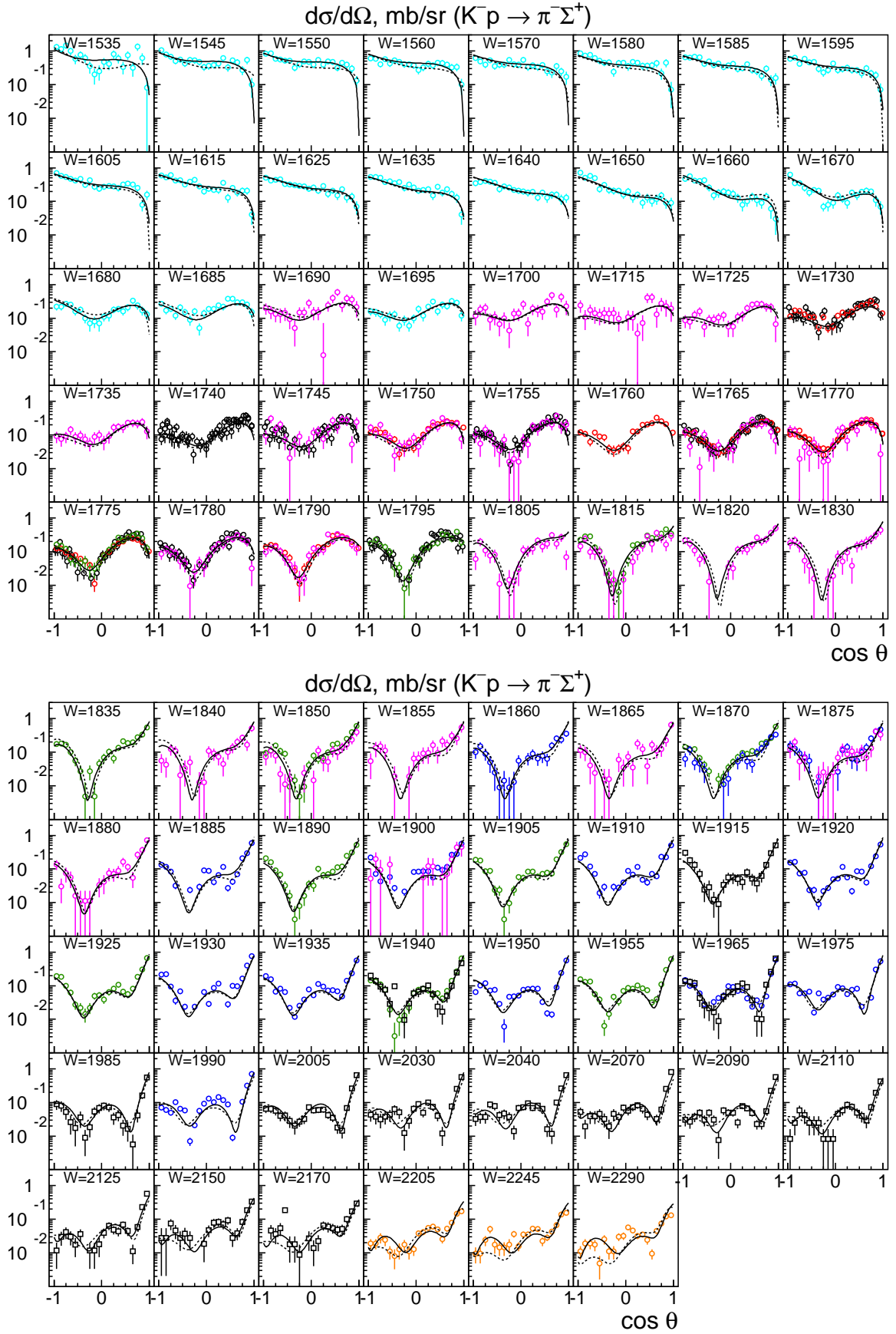


Fig. 12. Differential cross sections for $K^-p \rightarrow \pi^- \Sigma^+$. The data are from \circ [57], \circ [56], \circ [55], \circ [70], \circ [70], \circ [67], \square [75], \circ [76].

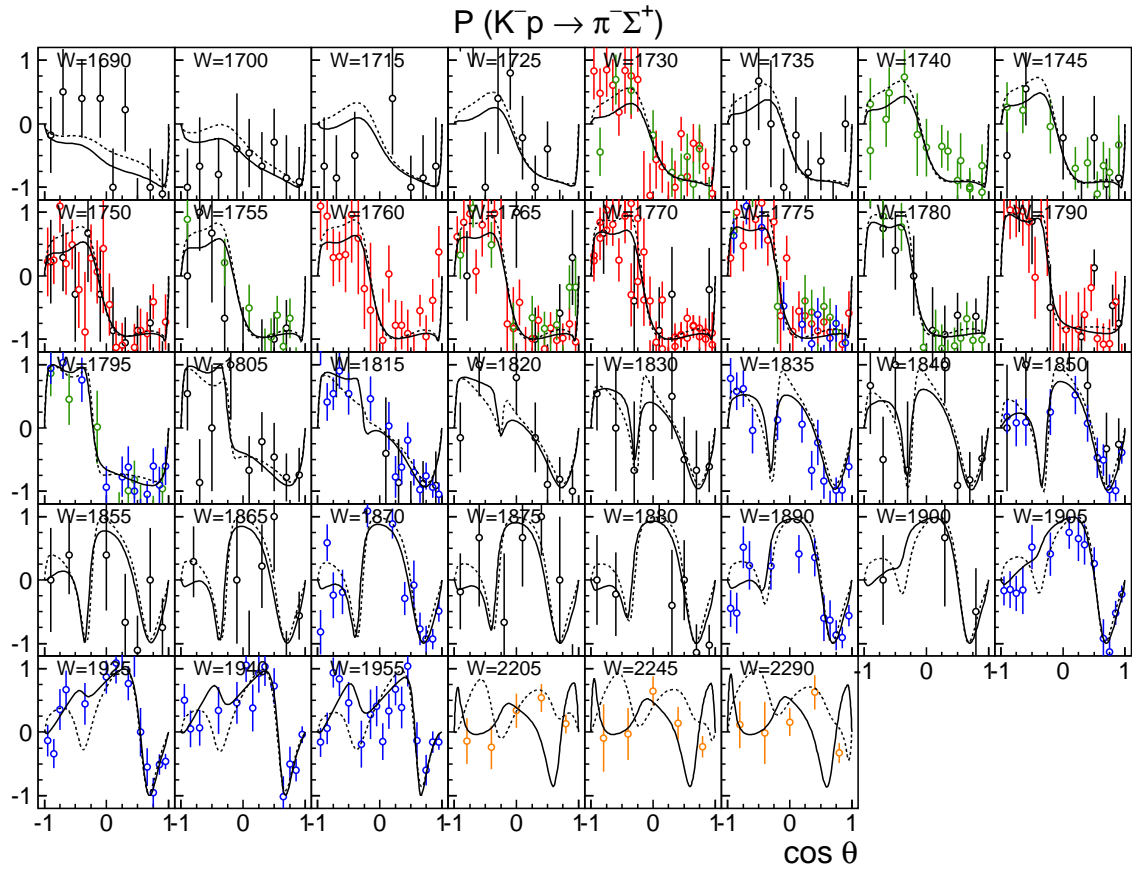


Fig. 13. P for $K^-p \rightarrow \pi^- \Sigma^+$. The data are from \circ [56], \circ [55], \circ [70], \circ [67], \circ [76].

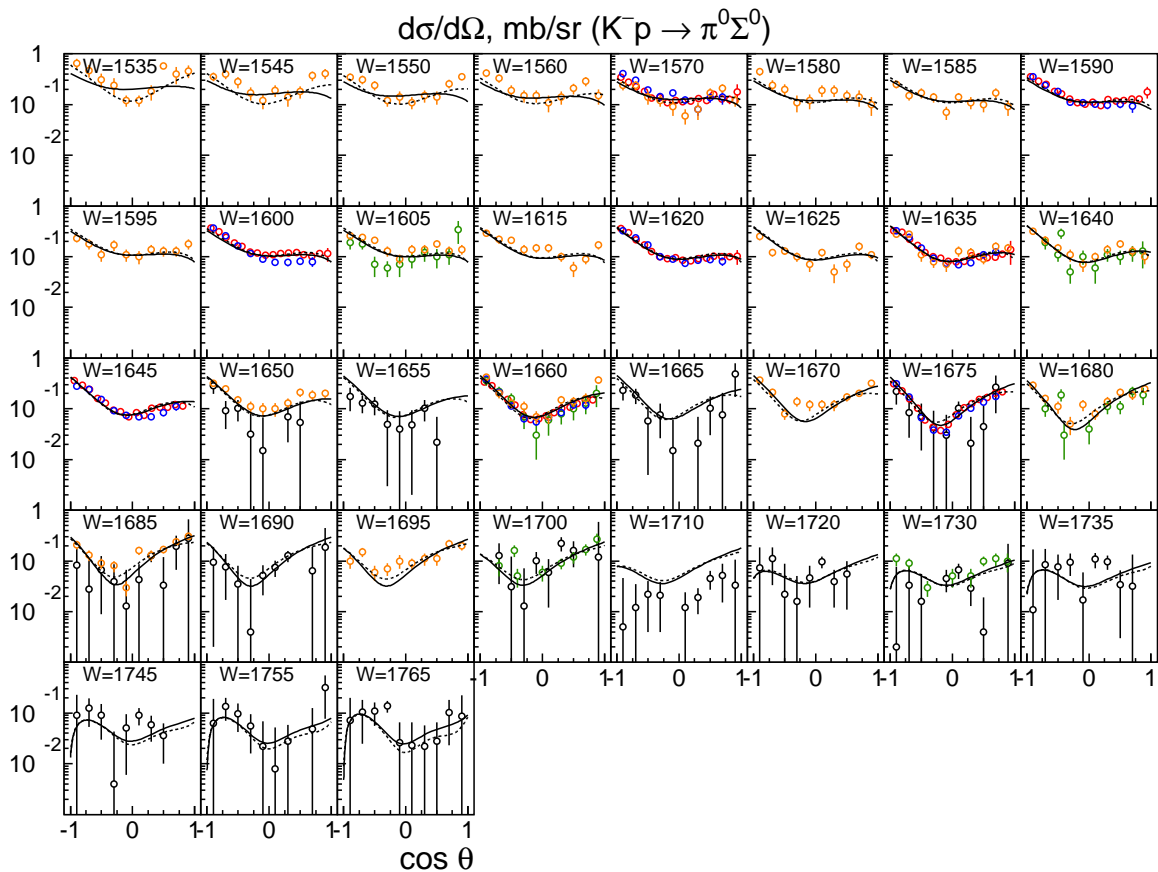


Fig. 14. Differential cross sections for $K^-p \rightarrow \pi^0 \Sigma^0$. Data: \circ [59], \circ [23], \circ [72], \circ [73], \circ [24].

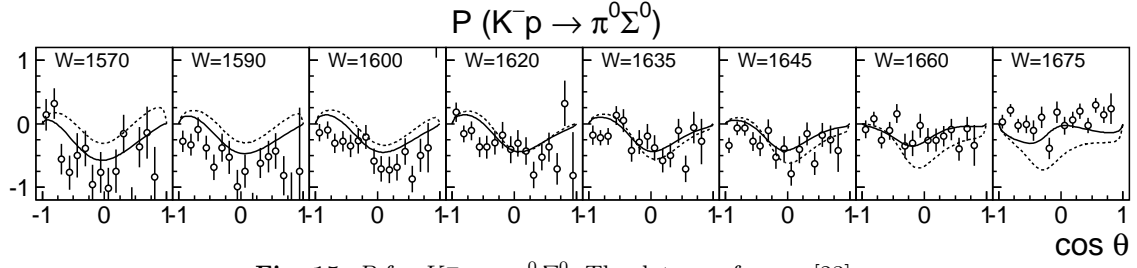


Fig. 15. P for $K^-p \rightarrow \pi^0 \Sigma^0$. The data are from \circ [23].

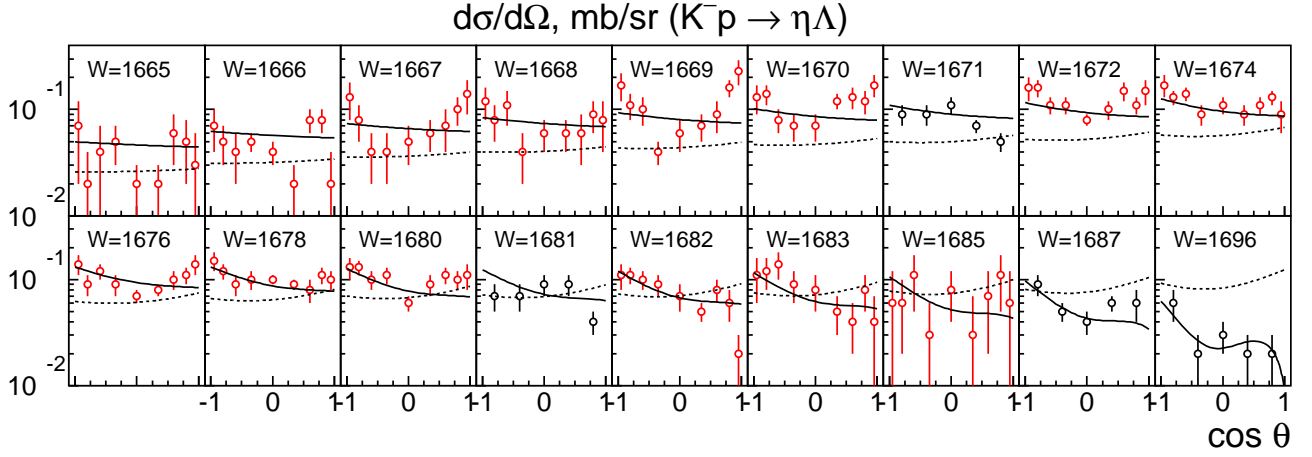


Fig. 16. Differential cross sections for $K^-p \rightarrow \eta \Lambda$. The data are from \circ [59], \circ [22].

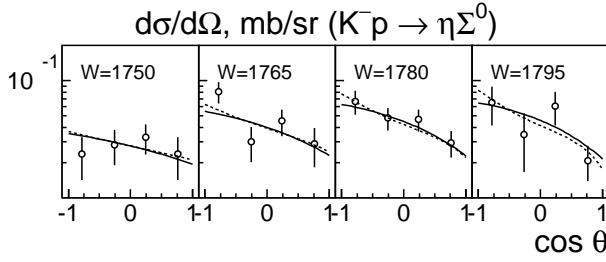


Fig. 17. Differential cross sections for $K^-p \rightarrow \eta \Sigma$. The data are from \circ [77]

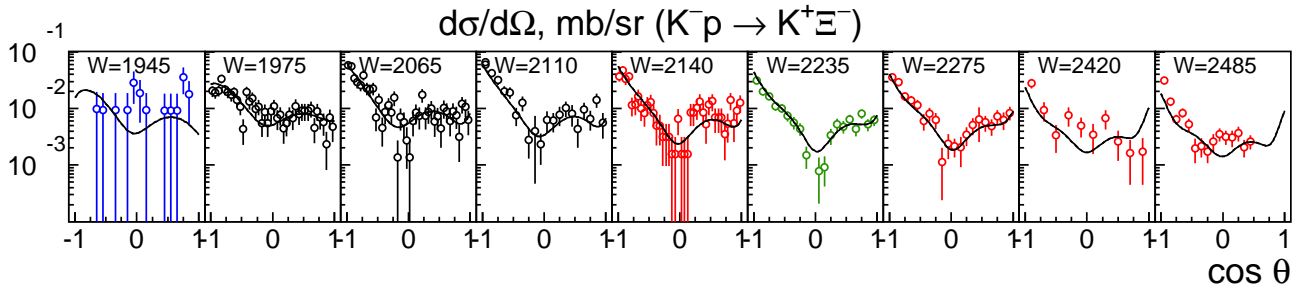


Fig. 18. Differential cross sections for $K^-p \rightarrow K^+ \Xi^-$. Data: \circ [79], \circ [80], \circ [83], \circ [84].

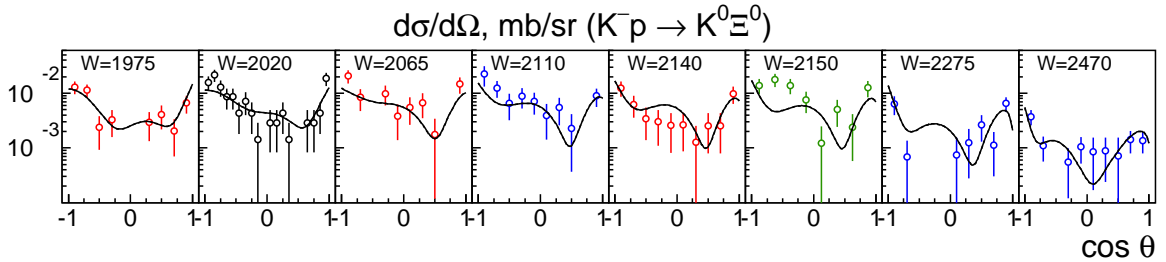


Fig. 19. Differential cross sections for $K^-p \rightarrow K^0 \Xi^0$. Data: \circ [78], \circ [79], \circ [80], \circ [81].

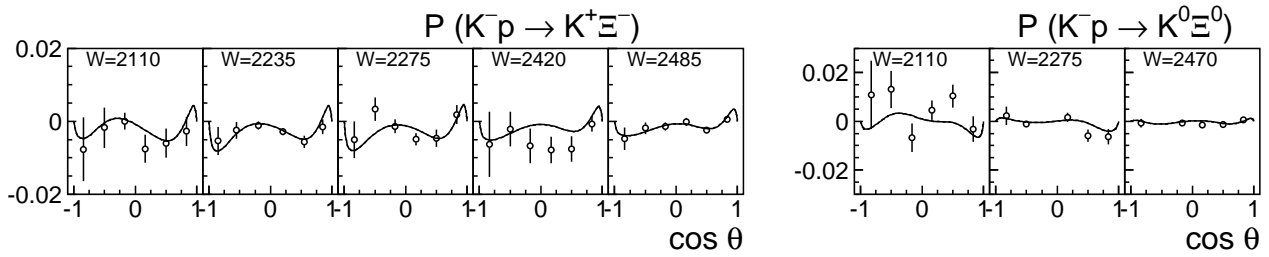


Fig. 20. Recoil asymmetry for $K^-p \rightarrow K^+\Xi^-$ and $K^-p \rightarrow K^0\Xi^0$. The data are from [90].

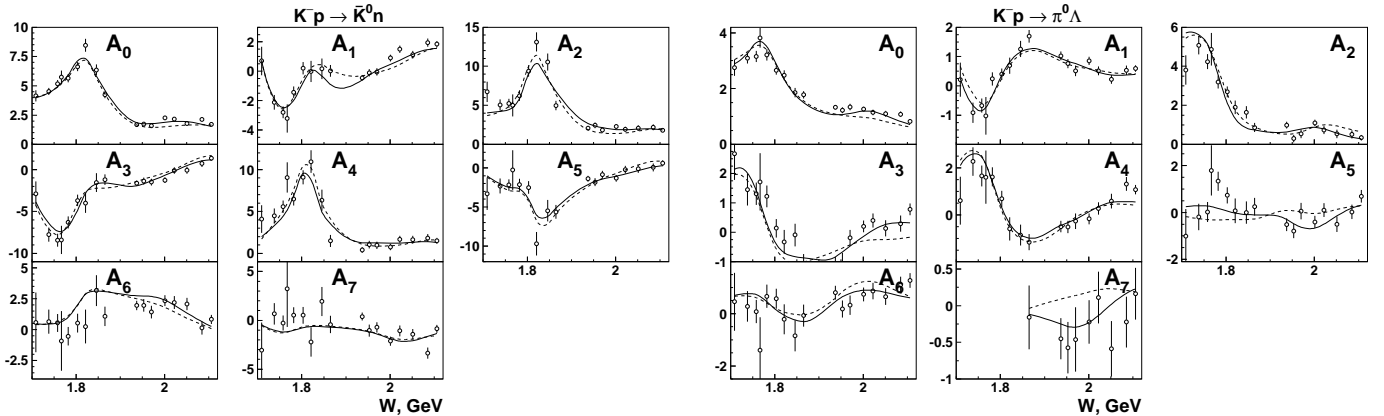


Fig. 21. Legendre coefficients for the expansion of the differential cross sections for $K^-p \rightarrow \bar{K}^0n$ (left) and $K^-p \rightarrow \pi^0\Lambda$ (right). The data are from [86].

forward direction and reaches 10 mb/sr while charge exchange leads to an oscillating cross section staying below 1 mb/sr. Obviously, there are significant t -channel contributions to the elastic channel – likely due to Pomeron exchange – while t -channel contributions to the charge-exchange reaction need ρ exchange. The impact of hyperon resonances is better seen in the charge-exchange data.

At the lowest mass – 1465 MeV – the charge-exchange cross section falls off slightly in forward direction; it is largely due to the dominant S -wave scattering with a small P -wave contribution. S -wave or P -wave alone would both lead to a constant angular distribution. At some masses, the reactions are dominated by one resonance. It may be helpful to compare the experimental angular distributions with the theoretical distributions (see Fig. 2) for a few mass intervals.

Figure 6 shows the angular distribution for $K^-p \rightarrow \bar{K}^0n$. At 1520 MeV, there is a clear $(3\cos^2\theta + 1)$ distribution above a very small background. A comparison with Fig. 2 shows that $J = 3/2$ is the dominant wave: of course, it is the well-known $\Lambda(1520)$. With increasing mass, the $J = 3/2$ contribution gets smaller and the minimum shifts without additional wiggles and without a strong forward-backward asymmetry. This pattern signals additional contributions from $J^P = 1/2^+$ and $J^P = 1/2^-$ waves.

At 1680 MeV, a sharp minimum is seen in the total $K^-p \rightarrow \bar{K}^0n$ cross section (see Fig. 22) which is assigned to a sign change of the amplitude in the $N\bar{K}$ S -wave amplitude at about this mass. $\Lambda(1670)1/2^-$ appears as a dip rather than as a peak (like $f_0(980)$ in $\pi\pi$ scattering). The

effect is enhanced by the sudden rising of the $\Lambda(1690)3/2^-$ contribution. Interestingly, the $K^-p \rightarrow \eta\Lambda$ cross section rises from threshold to a peak value of above 0.1 mb/sr at 1670 MeV and has fallen below 0.03 mb/sr in the highest-mass bin at 1696 MeV.

In the subsequent energy bins of the $K^-p \rightarrow \bar{K}^0n$ differential cross sections, a stronger forward-backward asymmetry develops which indicates the interference of odd and even partial waves. Gradually, the angular distribution develops a strong w-shaped distribution, best recognized in the 1820 to 1850 MeV mass bins. The comparison with Fig. 2 suggests significant $J = 5/2$ contributions. The partial wave analyses assigns this to a strong $\Lambda(1820)5/2^+$ production, the forward-backward asymmetry to a smaller $\Sigma(1775)5/2^-$ amplitude and some smaller contributions from lower partial waves. Above 2000 MeV, the angular distributions are characterized by forward and backward maxima with two additional maxima: In this mass region, $J^P = 7/2^\pm$ are the most prominent partial waves (see Fig. 2). Similar observations can be made for the reaction $K^-p \rightarrow \pi^0\Lambda$.

The differential cross sections for the processes $K^-p \rightarrow \pi^0\Lambda$ and the Λ polarization are shown in Figs. 8, 9, and 10, those for $K^-p \rightarrow \pi^0\Sigma^0$ and the Σ^0 polarization in Figs. 14 and 15. Only Σ^* resonances contribute to $K^-p \rightarrow \pi^0\Lambda$, and only Λ^* resonances to $K^-p \rightarrow \pi^0\Sigma^0$.

Inspecting Figs. 3, 4, 6, 7 again, we notice a few discrepancies between data and fit. Often, the discrepancies are enforced by data in neighboring bins: the structure at $\cos\theta = 0$ and 1935 MeV in Fig. 4 is, e.g., incompatible

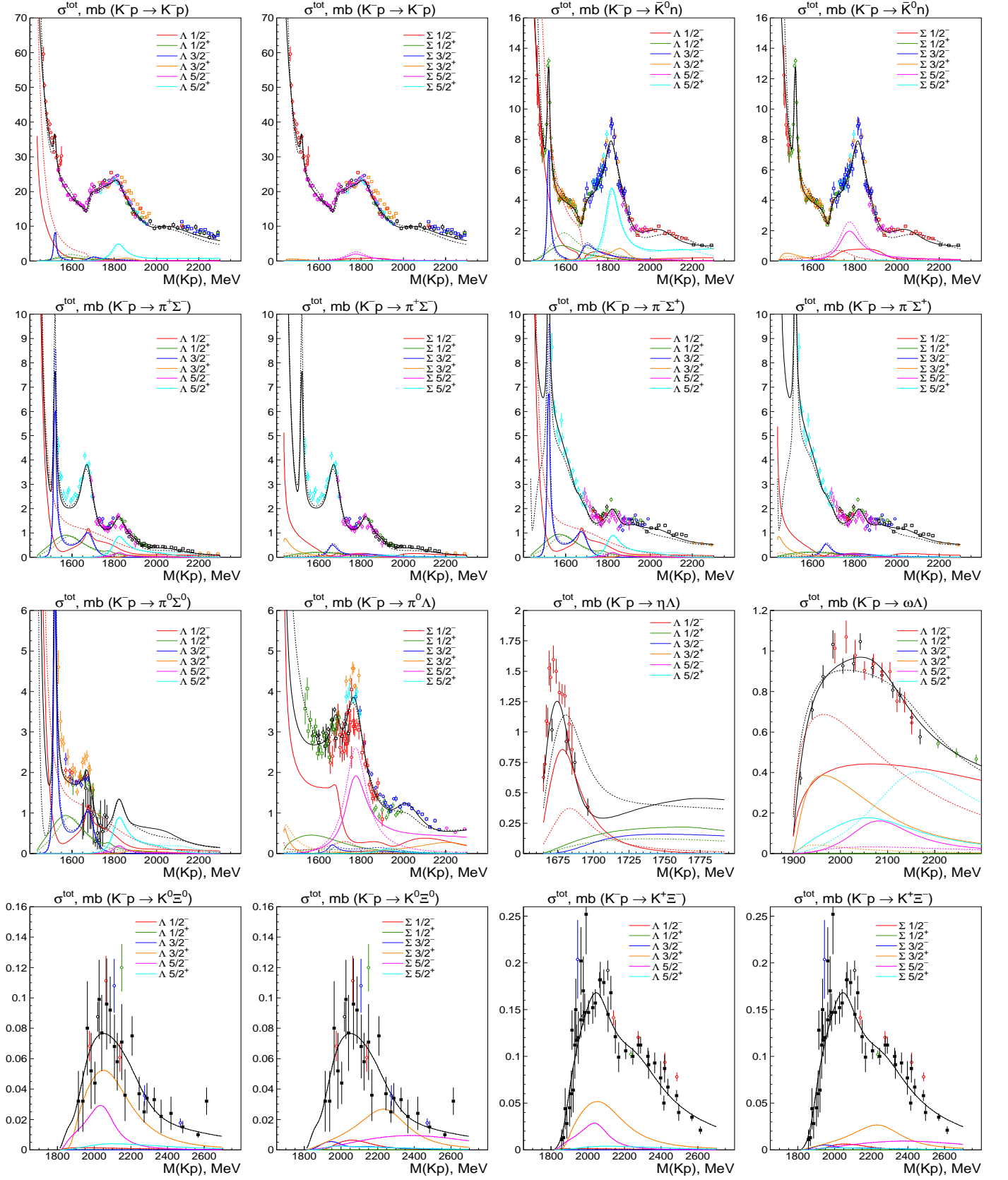


Fig. 22. Total cross sections for major K^- induced reactions. The data on the total cross sections are calculated from the corresponding differential cross sections. The black solid curves represent the result of the final coupled-channel fit, the dotted line shows the result of the primary Breit-Wigner fit. The partial wave contributions for Λ^* 's and Σ^* 's are shown in separate subfigures.

with the neighboring bins. The same statements holds for the data from [66] above 2200 MeV which are incompatible with those from [63] and [58].

The polarization data are shown in Fig. 5. Polarization data are available in the full energy range considered here even though above 2 GeV with limited statistical significance only. For a single partial wave, the polarization vanishes. The complicated angular dependence of P indicates the presence of several partial waves which makes a direct interpretation difficult. However, these data provide important constraints for the partial-wave analysis.

When the cross sections for $\pi^- \Sigma^+$ and $\pi^+ \Sigma^-$ production in Figs. 11 and 12 are compared, similar effects as in $\bar{K}N$ production are seen. The cross sections for $\pi^- \Sigma^+$ are larger and the angular distributions at high energies show forward peaking. Note that for t -channel exchange, $\pi^+ \Sigma^-$ production requires an exotic particle to be exchanged. It is not included in the fits and not required by the data. The contributing resonances are discussed using the data on $K^-p \rightarrow \pi^+ \Sigma^-$.

The branching ratios for $\Lambda(1520) \rightarrow \Lambda\pi\pi$, $\Sigma\pi\pi$ and $\Lambda\gamma$ of $(12 \pm 1)\%$ are imposed as missing width; the $\Lambda(1520) \rightarrow \pi\Sigma$ decay fraction is then fixed fixed by unitarity ($\Gamma_{\text{tot}} = \sum \Gamma_i$) when the data on elastic and charge exchange K^-p scattering are used; these data span the mass range down to ~ 1465 MeV.

The $\Lambda(1690)3/2^-$ can be recognized by the $(3 \cos^2 \theta + 1)$ angular distribution. The resonance makes a very significant contribution, jointly with $\Lambda(1670)1/2^-$. Both are even partial waves, and the angular distribution remains approximately symmetric. At masses above 1800 MeV, the w-shaped angular distribution turns up again, signalling $\Lambda(1820)5/2^+$ but with a forward-backward asymmetry due an odd partial wave from $\Lambda(1830)5/2^-$.

Data on the reaction $K^-p \rightarrow \pi^0 \Sigma^0$ were difficult to extract with the experimental techniques of the 70ties of last century: The Σ^0 decays to $\Lambda\gamma$; with $\pi^0 \rightarrow \gamma\gamma$, there are three γ in the final state. In [73], a bubble chamber was used that was filled with propane (C_3H_8) and freon (CF_3Br) in which γ ray have a high chance to convert. The γ conversion probability depends on the γ energy which was difficult to simulate. In view of these difficulties, the agreement between data and fit seems acceptable (see Fig. 14). The polarization P for this reaction (see Fig. 15) was determined using the Crystal Ball detector at BNL [23] with its excellent photon detection capability but with a limited energy range.

The first mass bin in Fig. 14 seems to suggest that there should be more $\Lambda(1520)$ than the fit admits. A larger $\Lambda(1520)$ contribution would, however, worsen the fit to the data on the $\pi^\mp \Sigma^\pm$ final states. In the 1650 to 1700 MeV mass range, a $(3 \cos^2 \theta + 1)$ contribution signals $\Lambda(1690)3/2^-$ contributions above a small even partial wave. The fit additionally identifies $\Lambda(1670)1/2^-$. Polarization data exist only over a very limited range.

The low-energy region of the $K^-p \rightarrow \pi^0 \Lambda$ differential cross section is dominated by the interference of even and odd partial waves, of S - and P -waves. At higher energies similar structures show up as we have seen them before:

first a $(3 \cos^2 \theta + 1)$, later a $9/4 \cdot (5 \cos^4 \theta - 2 \cos^2 \theta + 1)$ angular distribution distorted by contributions from other waves. At masses above 2000 MeV, more wiggles show up. The fit is sensitive to the polarization data but their statistical value is limited again.

The differential cross sections for $K^-p \rightarrow \eta\Lambda$ are shown in Figs. 17. They do not show striking structures.

The structure in the $K^-p \rightarrow K^+ \Xi^-$ differential cross section (Fig. 18) identifies leading contributions in the $J^P = 3/2^+$ and $3/2^-$ partial waves, the assignment to the Λ or Σ sector follows from the $K^-p \rightarrow K^0 \Xi^0$ channel (Fig. 19): $K^0 \Xi^0 \rightarrow \Sigma^0$ is forbidden. Description of the recoil asymmetry for both reactions is shown in Fig. 20. The two reactions were studied in a single-channel analysis [99]. Possibly contributing hyperon resonances were tested in a blindfold identification process. Ten resonances were suggested to contribute to the reaction, among them four 1^* resonances for which we find no evidence in any final state. The strongest evidence is seen for $\Sigma(2030)7/2^+$ which we do not observe in this decay mode.

The authors of Ref. [86] reported measurements of the charge exchange reaction and $\pi^0 \Lambda$ formation. The results were expanded into associated Legendre polynomials:

$$\frac{d\sigma}{d \cos \Theta} = \frac{1}{2} \sum_l A_l P_l^0(\cos \Theta) \quad (29)$$

The data were included in our fits. The data are shown in Fig. 21. Significant structures are seen, in particular for $K^-p \rightarrow \bar{K}^0 n$ at 1800 MeV where the interference of $\Lambda(1800)1/2^-$, $\Lambda(1820)5/2^+$, $\Lambda(1830)5/2^-$ leads to a complicated pattern. The largest contributions in $K^-p \rightarrow \pi^0 \Lambda$ are at about 1700 MeV which are strongly influenced by $\Sigma(1620)1/2^-$, $\Sigma(1660)1/2^+$, $\Sigma(1670)3/2^-$. With S , P , and D -waves, the Legendre coefficients up to A_4 show traces of these resonances while A_5 , A_6 and A_7 stay small.

4 Mass scans

In the second step, we searched for new resonances and performed scans. In these *exploratory* fits, the resonances were described by relativistic Breit-Wigner amplitudes. States rated with three and four stars in the RPP were assumed to exist and used in all fits. In the mass scans, the masses of further states were scanned one by one in the corresponding mass regions. Figure 23 shows the first series of scans. The *primary* fit contained five positive and seven negative-parity Λ resonances and four negative and four positive-parity Σ resonances in the $J^P = 1/2^\pm, 3/2^\pm, 5/2^\pm$ and $7/2^\pm$ partial waves. In the scan, we added one resonance and varied its mass in steps. At each step, a full fit to the data was performed and the χ^2 of the fit recorded. The χ^2 's as functions of the imposed mass vary from fit to fit; sometimes a significant improvement is observed. The minimum defines a possible candidate for an additional resonance.

In the case of scan for an additional positive-parity Λ resonance, the deepest minimum is seen in the scan of the

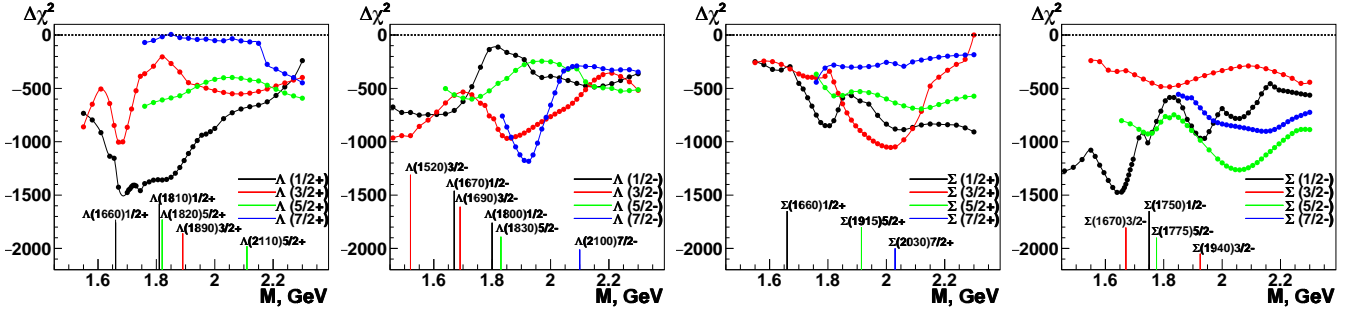


Fig. 23. The scan of the primary fit for additional resonances. The three vertical lines indicate the position of resonances which were assumed to exist. The mass of one additional resonance is stepped through the mass range and the χ^2 of the fit is monitored.

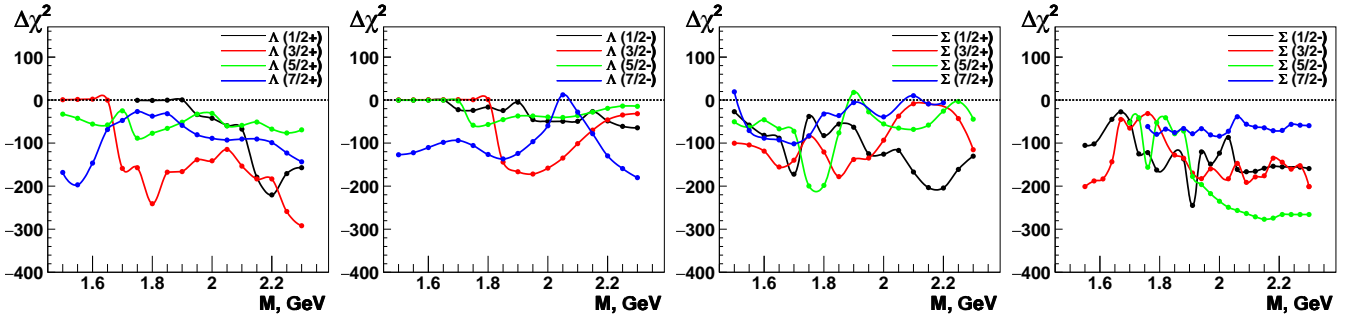


Fig. 24. Final scans for additional resonances. The scale shows the improvement of $\Delta\chi^2$ calculated from the final solution. The final fit uses the formalism described in section 2, the resonances scanned are parametrized as Breit-Wigner resonances.

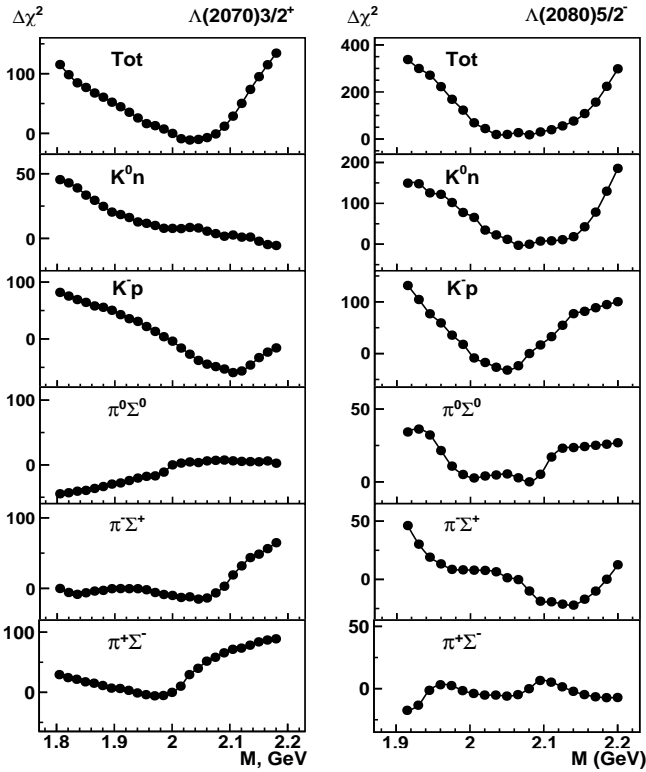


Fig. 25. Scan of the $\Lambda(2070)3/2^+$ and $\Lambda(2080)5/2^-$ states from the solution with all states identified.

$J^P = 1/2^+$ -wave. The minimum is rather broad and indicates that more resonances could be required. In further fits, no significant structure in this partial waves survives. The minimum in the $3/2^+$ wave is fake: the minimum is entirely due to the data on $K^-p \rightarrow \pi^0\pi^0\Lambda$ [25] at the transition from one momentum to the next momentum. In the scan for a $J^P = 7/2^-$ Λ resonance, a narrow minimum is seen at about 1930 MeV which would be a rather low mass for a $7/2^-$ -resonance. It is kept for further investigations, and is finally not confirmed. Furthermore, there are indications for a $J^P = 3/2^-$ state at about 1870 MeV. In the scans for positive-parity Σ resonances, we keep a $1/2^+$ at 1780 MeV and a $3/2^+$ at 2000 MeV for further investigations. The scan of the $J^P = 1/2^-$ -wave for Σ resonances, a very significant minimum at 1670 MeV is seen even though a $\Sigma(1670)1/2^-$ resonance is already included in the *primary* fit. In the $5/2^-$ -wave, a second minimum is seen at 2080 MeV. However, this minimum faded away in further studies.

These preliminary fits demonstrate that significant minima can be seen in fits but that the minima do not necessarily correspond to true physical states. For the analysis presented here, we performed several thousand fits with different hypotheses. At the end, we had a set of resonances which improved the χ^2 by more than 400 units. This is called our *final* fit. These resonances will be discussed below (see Table 8).

A search for a further resonance – beyond those listed in Table 8 – led to residual fluctuations of less than 300 in χ^2 . Figure 24 shows the scans for positive and negative-parity Λ and Σ resonances. Some candidates could exist which improve χ^2 by about 200 or more: There might be one broad or two unresolved Λ candidates with $3/2^-$ in the 1800 to 2100 MeV range, or a $7/2^-$ and a $3/2^+$ Λ candidate above 2300 MeV. There are indications for a Λ $3/2^+$ candidate at 1800 MeV, a $\Sigma(2180)1/2^+$ and a Σ candidate with $5/2^+$ at 1775 MeV and a $5/2^-$ Σ candidate above 2100 MeV. The χ^2 minimum in the Σ $1/2^-$ scan at 1900 MeV might indicate that the description of $\Sigma(1900)1/2^-$ is not perfect. We do not consider any of these residual minima as statistically significant.

Figure 25 shows the final scans of two new Λ states after all resonances have been identified. The mass scan of $\Lambda(2080)5/2^-$, e.g., shows a deeper minimum than the $\Lambda(2070)3/2^+$ state although the drop of the latter state has a more significant effect for the data description. $\Lambda(2070)3/2^+$ is significantly broader and it influences the via interference with other waves over a wider range. There is no clear minimum of $\Lambda(2070)3/2^+$ in any reaction: the global minimum is due to a χ^2 function decreasing with mass for $K^-p \rightarrow \bar{K}N$ and increasing for $K^-p \rightarrow \pi\Sigma$. When this behavior is observed, we assign at most 1^* to the resonance. The 3^* and 4^* resonance show clear minima for several final states.

5 The final fit

While the primary fit uses a Breit-Wigner description for the contributing resonances, the final fit uses the multi-channel K-/D-matrix-formalism described in Section 2. Figure 22 exhibits the total cross sections and the partial wave contributions determined in the *primary* and the *final* fit. The total cross sections are shown twice: the contributions from Λ resonances are shown on the left figures, those from Σ resonances on the right figures. Interferences between different partial waves – which play an important role in the analysis – do not contribute to the total cross section. Of relevance for the total cross section are on the other hand interferences of different isospin contributions in the same partial wave, which are not shown. Contributions from t - and u -channel exchanges are also not shown: This is the reason why, e.g., the sum of the resonant contributions for K^-p elastic scattering is much less than the total cross section. The χ^2 contributions from the individual data sets are listed in Tables 2 to 5. While the χ^2 's for the *primary* fit are already acceptable, they are considerably improved when additional resonances are included. Some data are perfectly described in the final fit, other data contribute with a large χ^2 . One has, however, to have in mind that the data often are not fully consistent. Thus a χ^2 of one per degree of freedom cannot be expected.

In Table 7 we compare our χ^2 's with those obtained by the ANL-Osaka group. We use the same data but in several cases, our data set is slightly extended. Yet, for the polarization observable in $K^-p \rightarrow \pi^0\Sigma^0$, we use only one

Table 7. Comparison of the data base and the best χ^2 for the ANL-Osaka fits in their model A, their model B, and the final BnGa fit. The fits of the Legendre coefficients extracted from differential cross section and density matrix elements are marked with (LC).

	ANL-Os. N_{data}	BnGa	Model A/B χ^2/N_{data}	BnGa
$K^-p \rightarrow K^-p$				
$d\sigma/d\Omega$	3962	5170	3.07 / 2.98	1.80
P	510	1180	2.04 / 2.08	1.41
$K^-p \rightarrow \bar{K}^0n$				
$d\sigma/d\Omega$	2950	3445	2.67 / 2.75	1.55
$d\sigma/d\Omega$ (LC)		134	/	1.86
$K^-p \rightarrow \pi^-\Sigma^+$				
$d\sigma/d\Omega$	1792	2455	3.37 / 3.49	1.45
P	418	593	1.30 / 1.28	2.09
$K^-p \rightarrow \pi^0\Sigma^0$				
$d\sigma/d\Omega$	580	691	3.68 / 3.50	1.96
P	196	124	6.39 / 5.80	2.41
$K^-p \rightarrow \pi^+\Sigma^-$				
$d\sigma/d\Omega$	1786	2082	2.56 / 2.18	1.59
$K^-p \rightarrow \pi^0\Lambda$				
$d\sigma/d\Omega$	2178	2478	2.59 / 3.71	1.66
P	693	892	1.41 / 1.73	1.25
$K^-p \rightarrow \eta\Lambda$				
$d\sigma/d\Omega$	160	160	2.69 / 2.03	1.50
P	18	—	0.94 / 3.83	—
$K^-p \rightarrow K^0\Xi^0$				
$d\sigma/d\Omega$	33	67	1.24 / 1.61	0.89
σ_{tot}		16	/	1.00
P		11	/	1.70
$K^-p \rightarrow K^+\Xi^-$				
$d\sigma/d\Omega$	92	193	2.05 / 1.74	1.31
σ_{tot}		29	/	1.57
P		18	/	0.93
$K^-p \rightarrow \Lambda\omega$				
$d\sigma/d\Omega$	—	300	— / —	1.03
$\rho_{00}, \rho_{10}, \rho_{1-1}$ (LC)	—	158	— / —	1.30

of two existing data sets [23, 24]. When both data sets were excluded from the analysis, the predicted polarization was close to the values from [23] and disagreed with [24]. Hence we decided not to use the latter data.

Due to a larger number of resonances, the BnGa fit achieves a better χ^2 even though more data are used. The Kent [7] and Carnegie-Mellon [11] groups do not report the χ^2 's achieved in their fits.

Table 8. Resonances found to contribute to K^- induced reactions. The columns give the Breit-Wigner mass and width, and the increase of χ^2 when a hyperon is removed from the fit, and our evaluation of the star rating. The small numbers give the PDG entries. Some 4* resonances cannot be removed from the fit without destroying the fit; $\delta\chi^2 > 10\,000$ is given for these resonances. A statistically significant very broad enhancements in the $J^P = 1/2^-$ wave are likely due to some background and not considered as true resonances. ¹: no estimate given in the RPP; our own estimate.

	Mass	Width	$\Delta\chi^2$	Status		Mass	Width	$\Delta\chi^2$	Status
$\Lambda(1405)1/2^-$	1420 ± 3 1405.1 ^{+1.3} _{-1.0}	46 ± 4 50.5 \pm 2.0	4070	****	$\Sigma(1620)1/2^-$	1681 ± 6 ≈ 1620	40 ± 12 10 to 400	386	(*) *
$\Lambda(1670)1/2^-$	1677 ± 2 1660 to 1680	33 ± 4 25 to 50	3610	****	$\Sigma(1750)1/2^-$	1692 ± 11 1730 to 1800	208 ± 18 60 to 160	3032	**** ***
$\Lambda(1800)1/2^-$	1811 ± 10 1720 to 1850	209 ± 18 200 to 400	1896	***	$\Sigma(1900)1/2^-$	1938 ± 12 1900 \pm 21	155 ± 30 191 \pm 47	1500	** *
$\Lambda(1520)3/2^-$	1518.5 ± 0.5 1519.5 \pm 1.0	15.7 ± 1.0 15.6 \pm 1.0	>10 000	****	$\Sigma(2160)1/2^-$	2165 ± 23	320^{+300}_{-60}	1612	* new
$\Lambda(1690)3/2^-$	1689 ± 3 1685 to 1695	75 ± 5 50 to 70	>10 000	****	$\Sigma(1670)3/2^-$	1665 ± 3 1665 to 1685	54 ± 6 40 to 80	5894	**** ****
$\Lambda(1830)5/2^-$	1821 ± 3 1810 to 1830	64 ± 7 60 to 110	1790	***	$\Sigma(1940)3/2^-$	1878 ± 12 1900 to 1950	224 ± 25 150 to 300	1708	*** ***
$\Lambda(2080)5/2^-$	2082 ± 13 -	181 ± 29 -	770	* new	$\Sigma(2000)3/2^-$	2005 ± 14 -	178 ± 23 -	446	* new
$\Lambda(2100)7/2^-$	2090 ± 15 2090 to 2110	290 ± 30 100 to 250	5412	****	$\Sigma(1775)5/2^-$	1776 ± 4 1770 to 1780	124 ± 8 105 to 135	>10 000	**** ****
$\Lambda(1600)1/2^+$	1605 ± 8 1560 to 1700	245 ± 15 50 to 250	>10 000	****	$\Sigma(2100)7/2^-$	2146 ± 17 ≈ 2100	260 ± 40 50 to 150 ¹	666	* *
$\Lambda(1890)3/2^+$	1873 ± 5 1850 to 1910	103 ± 10 60 to 200	4480	****	$\Sigma(1660)1/2^+$	1665 ± 20 1630 to 1690	300^{+140}_{-40} 40 to 200	1870	*** ***
$\Lambda(2070)3/2^+$	2070 ± 24 -	370 ± 50 -	1144	* new	$\Sigma(2230)3/2^+$	2240 ± 27	345 ± 50	1200	* new
$\Lambda(1820)5/2^+$	1822 ± 4 1815 to 1825	80 ± 8 70 to 90	>10 000	****	$\Sigma(1915)5/2^+$	1918 ± 6 1900 to 1935	102 ± 12 80 to 160	2002	**** ****
$\Lambda(2110)5/2^+$	2086 ± 12 2090 to 2140	274 ± 25 150 to 250	1418	** ***	$\Sigma(2030)7/2^+$	2032 ± 6 2025 to 2040	177 ± 12 150 to 200	2856	**** ****

Finally, we give in Table 8 a list of the hyperon resonances which we use in the fits. One Λ resonance is not listed. We find a very broad Λ resonance with $J^P = 1/2^-$ at 2230 MeV with a width of ≈ 450 MeV. It is statistically significant; according to the criteria described in Section 6, it would be listed with three stars. Due to its large width, we think the resonance may hide a number of resonances with different spin and parities. Hence we do not include it in Table 8. A similar resonance shows up in the Σ sector. The $\Sigma(2160)1/2^-$ may have a width of up to 600 MeV and may also cover the contribution of several resonances. It could, however, also have a width of 260 MeV; that is the reason that we include this resonance in the listings. But due to this uncertainty, we assign only one star to it even this its statistical evidence would justify three stars.

There are several one-star resonances for which we see no evidence underlying their weakness in kaon-induced reactions. Most four and three-star resonances are confirmed.

Compared to our expectation of seven Λ^* and seven Σ^* resonances with negative parity and below ≈ 1900 MeV, we were missing one resonance in both sectors. The expected $3/2^-$ companion of $\Lambda(1800)1/2^-$ and $\Lambda(1830)5/2^-$ is definitely not seen, see the discussion in Section 4. In the Σ^* sector, a low-mass partner of $\Sigma(1670)3/2^-$ with $J^P = 1/2^-$ is missing. There is a 1* candidate $\Sigma(1620)1/2^-$. If we include this in the fit, the χ^2 gain is 386, just below our limit at 400 (see below). Thus we keep it as 1* resonance. Its mass of 1681 MeV is unexpectedly close to $\Sigma(1750)1/2^-$ which we find at 1692 MeV. We notice

that the K-matrix poles of the three low-mass Σ^* resonances with $J^P = 1/2^-$ are 1610, 1695, and 1900 MeV. In the nucleon sector, it had turned out that the helicity amplitudes for photoexcitation of $N(1535)1/2^-$ and $N(1650)1/2^-$ off protons and neutrons determined at the K-matrix pole [100] agree very well with expectations of the Single-Quark-Transition-Model [101] and are at variance with SU(3) relations at the T-matrix poles [102].

6 Hyperon resonances and their star rating

The final fit converged with a χ^2 minimum at $\chi^2 = 40615$. Table 8 lists the resonances used in the fit, their masses and widths. From the full list of resonances used to fit the data we removed individual resonances one by one. The new fit with readjusted parameters deteriorated, the increase in χ^2 is used to estimate the significance of the resonance. When some dominant 4* resonances were removed, the fit became very bad. In these cases we did not try to improve the fit but just left these resonances with their 4* rating.

In the RPP - not counting $\Lambda(1116)$, $\Sigma(1193)$, and $\Sigma(1385)$, there are at present 12 Λ and Σ resonances with 4*'s. We use these resonances to define criteria to estimate the star rating of resonances. In our analysis, the least significant 4* resonances are $\Lambda(1830)5/2^-$ and $\Sigma(1915)5/2^+$; when removed they led to an increase in χ^2 of 1790 or 2002, respectively. Since we do not wish to drastically alter the criteria for the star rating, we assign a 4* rating to resonances for which a χ^2 change of more than 2000 is observed. Thus 11 of the 12 4*-star resonances kept their star rating. We defined 400 as the minimum χ^2 change to accept a resonance with 1*. The ratings are thus defined by

$$\begin{aligned} 1* : 400 < \delta\chi^2 < 1000; & \quad 2* : 1000 < \delta\chi^2 < 1500; \\ 3* : 1500 < \delta\chi^2 < 2000; & \quad 4* : 2000 < \delta\chi^2. \end{aligned} \quad (30)$$

We do not observe any evidence for the low-mass Σ ‘‘bumps’’ at 1480, 1560, 1620, 1670, or 1690 MeV, observed in production experiments, and no evidence for the 1* $\Sigma(1580)3/2^-$ in agreement with the authors of Ref. [103]. Below 2200 MeV, we find no evidence for the 1* resonances $\Sigma(1620)1/2^-$, $\Sigma(1730)3/2^+$, $\Sigma(1770)1/2^+$, $\Sigma(1840)3/2^+$, $\Sigma(1940)3/2^+$, $\Sigma(2000)1/2^-$, $\Sigma(2070)5/2^+$, and no evidence for the 2* $\Sigma(1880)1/2^+$ and $\Sigma(2080)3/2^+$. We do not observe the 1* resonances $\Lambda(1710)1/2^+$, $\Lambda(2000)$, $\Lambda(2020)7/2^+$, and $\Lambda(2050)3/2^-$. $\Lambda(1810)1/2^+$ is the only 3* resonance for which we find no evidence. If we include it, the χ^2 improves by 106 units only, and mass and width are fitted to $M=1773\pm 7$; $\Gamma=39\pm 15$ MeV. Two resonances above 2230 MeV are included in the analysis but are not included in Table 8.

The changes in star rating suggested here are collected in Table 9. The most significant changes are suggested for resonances which so far had a 1* or 2* rating. Most of them are not seen here. The changes suggested for 3* and 4* resonances are moderate. Five new 1*-resonances are suggested.

Table 9. Suggested changes in star rating (the octet and decuplet ground states are not included in the counting). Two states, $\Sigma(1620)1/2^-$ and $\Lambda(1810)1/2^+$, we keep as one star resonances, even though they cannot be confirmed by our fits (see text and [30]).

	0*	1*	2*	3*	4*
4* to	-	-	-	1	11
3* to	-	1	1	3	2
2* to	4	-	-	-	-
1* to	12	2	2	-	-
new	-	5	-	-	-

In most cases, the fits finds a minimum within the mass-boundaries of the RPP, except for four exceptions: We find $\Sigma(1620)1/2^-$ at 1681 ± 6 MeV and $\Sigma(1750)1/2^-$ at 1692 ± 11 MeV, these two resonances are very close in mass and the evidence for the lower mass state is weak as discussed in the previous section. $\Sigma(1940)3/2^-$ is found at 1878 ± 12 MeV. In the $3/2^-$ partial waves, a new resonance is found, and it is not surprising that the masses of known resonances are shifted. In addition the $\Lambda(1405)$ is found at 1420 ± 3 MeV. This state is discussed in detail in [32].

Finally, we made *error defining fits*. We chose solutions with an additional resonance and a local minimum as shown in Figs. 24. From the spread of results we estimated the errors given to masses, widths and other properties (see [30]).

7 Partial wave amplitudes

Our partial wave amplitudes are not derived from energy-independent fits (i.e. from fits in slices of energy). Measurements of the spin-rotation parameters – needed for a truly energy-independent analysis – do not exist. The Kent group succeeded nevertheless to construct the amplitudes by first determining the leading waves and then defining the smaller ones. Our amplitudes are determined from energy-dependent fits to the differential cross sections and polarization data. As discussed above, we have made numerous fits, in particular also a large number of fits with different resonance contents. Some additional poles led to a small χ^2 reduction, of less than 400. For these fits, all partial wave amplitudes were determined as well. Thus, we derived a set of partial wave amplitudes which all are about consistent with the data. The spread of these results were used to determine a band for each partial wave amplitude.

Figures 26 and 27 show the real and imaginary parts of the partial wave amplitudes for $\bar{K}N$ elastic scattering in the two isospin channels, for the isospin 1 $\bar{K}N \rightarrow \pi\Lambda$ scattering and for the two isospins in $\bar{K}N \rightarrow \pi\Sigma$ determined in this analysis and in Refs. [6] and [8]. Giving the limitations of the data, the comparison shows reasonable consistency, at least for the leading contributions. The partial waves are very similar in all four solutions where strong resonances like $\Lambda(1520)3/2^-$, $\Lambda(1820)5/2^+$,

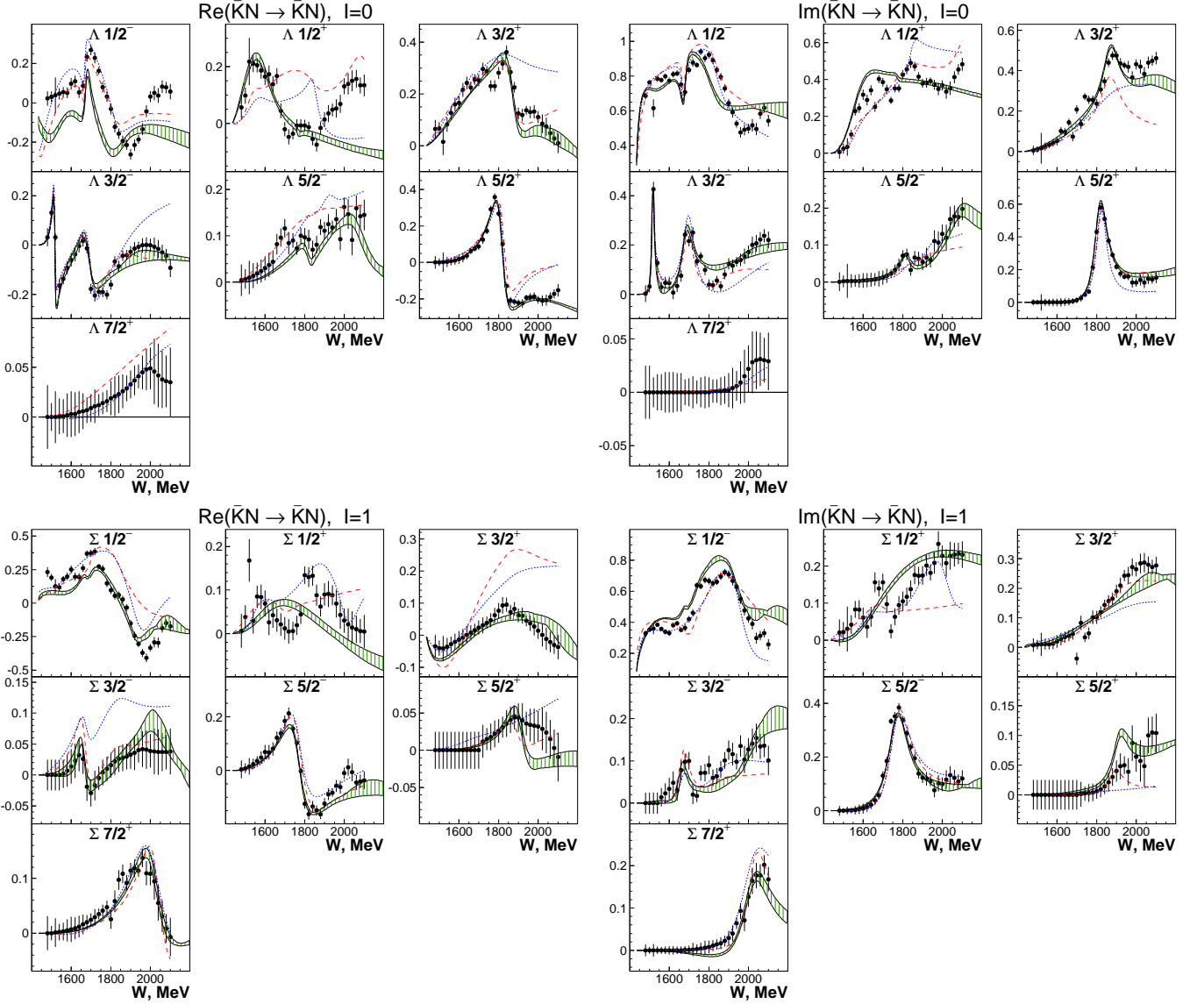


Fig. 26. Real and imaginary parts of K^-p induced scattering amplitudes. The solid points with error bars are the energy independent amplitudes derived in [6]. The larger part of the data used in [6] were fitted by the authors of Ref. [8]. Their amplitudes for solution A and B are given as short-dashed blue and long-dashed red curves. The green-shaded area represents the spread of results from our main solutions and from solution weak resonances turned off.

$\Lambda(1830)5/2^-$, $\Sigma(1670)3/2^-$, $\Sigma(1775)5/2^-$, $\Sigma(1915)5/2^+$, or $\Sigma(2030)7/2^+$ dominate the partial waves. For $\Lambda(1600)1/2^+$, the imaginary part is similar in all four analyses while the real part of analysis [6] deviates. The $\Lambda(1600)1/2^+$ low-mass amplitudes for $\bar{K}N \rightarrow \pi\Sigma$ from [6] and [8] are consistent but inconsistent with our findings. However, a significant $\Lambda(1670)1/2^-$ structure is seen in all analyses.

Above the lowest-mass resonance, the structure of the amplitudes shows significant differences. This is to be expected since the resonance content of the four analyses is different. To resolve these discrepancies, new data are likely mandatory.

8 Summary

We have collected existing data on hyperon formation in K^-p elastic and inelastic scattering. The data were fitted in a coupled-channel analysis within the BnGa framework. We looked systematically for contributing resonances in a large number of fits and mass scans. The statistical significance of all resonances was evaluated. We find five new resonances; some resonances are suggested to be upgraded others to be downgraded. For eighteen resonances – mostly listed as 1^* or 2^* resonances – we did not find any signature. The partial-wave amplitudes derived in our fits are compared to those from other analyses.

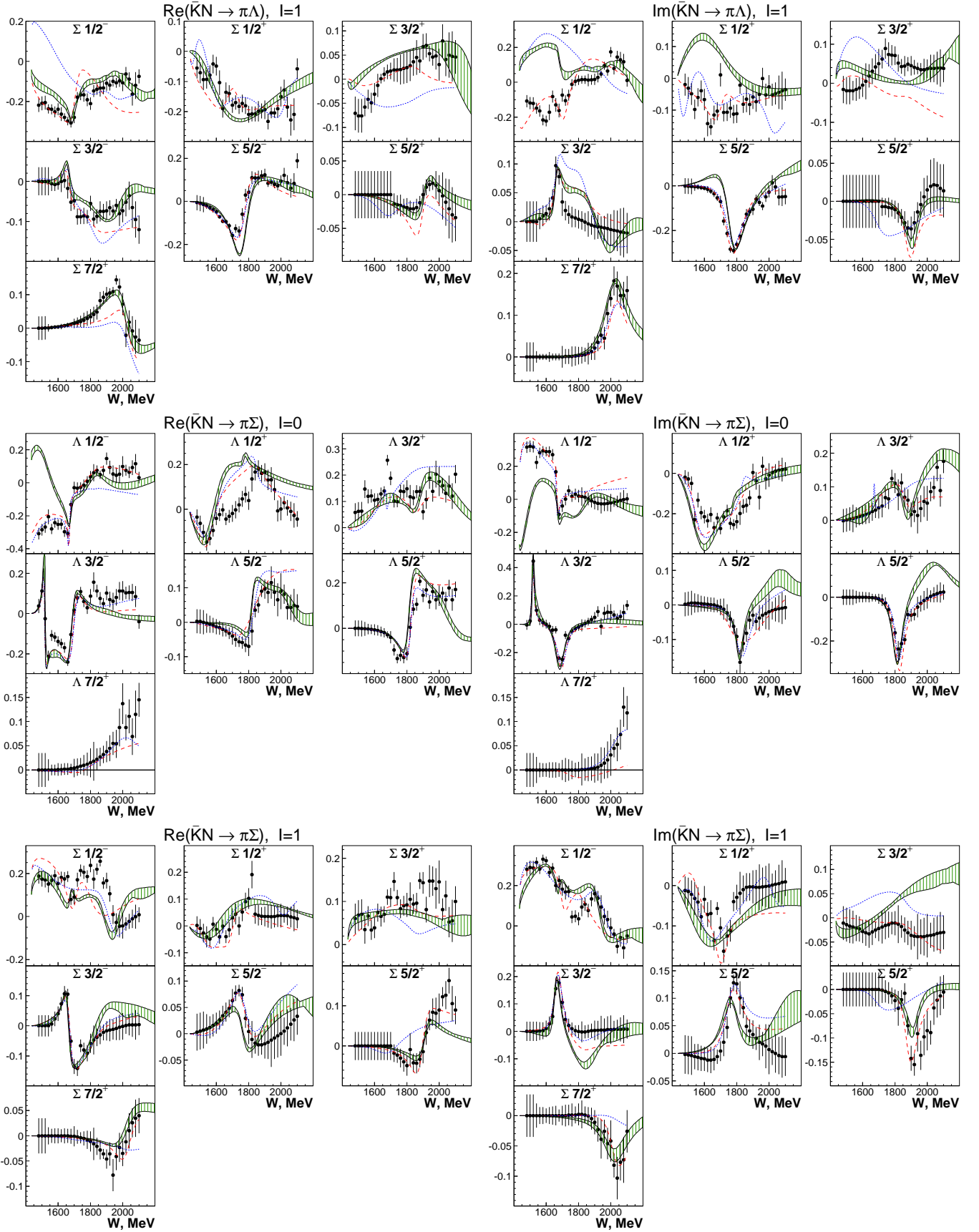


Fig. 27. Real and imaginary parts of K^-p induced scattering amplitudes. The solid points with error bars are the energy independent amplitudes derived in [6]. The larger part of the data used in [6] were fitted by the authors of Ref. [8]. Their amplitudes for solution A and B are given as short-dashed blue and long-dashed red curves. The green-shaded area represents the spread of results from our main solutions and from solution with weak resonances turned off.

Acknowledgements

We are very grateful to Sergey Prakhov for providing to us the Crystal Ball data on the $K^-p \rightarrow \pi^0\pi^0\Lambda$ and $K^-p \rightarrow \pi^0\pi^0\Sigma$ reactions. Comments by D. M. Manley and H. Kamano are kindly acknowledged. This work was supported by the *Deutsche Forschungsgemeinschaft* (SFB/TR110) and the *Russian Science Foundation* (RSF 16-12-10267).

References

1. E. Klempt and J. M. Richard, *Rev. Mod. Phys.* **82**, 1095 (2010).
2. V. Crede and W. Roberts, *Rept. Prog. Phys.* **76**, 076301 (2013).
3. N. Isgur and G. Karl, *Phys. Lett.* **72B**, 109 (1977).
4. N. Isgur and G. Karl, *Phys. Rev. D* **19**, 2653 (1979) Erratum: [*Phys. Rev. D* **23**, 817 (1981)].
5. M. Tanabashi *et al.* [Particle Data Group], *Phys. Rev. D* **98**, no. 3, 030001 (2018).
6. H. Zhang, J. Tulpan, M. Shrestha and D. M. Manley, *Phys. Rev. C* **88**, no. 3, 035204 (2013).
7. H. Zhang, J. Tulpan, M. Shrestha and D. M. Manley, *Phys. Rev. C* **88**, no. 3, 035205 (2013).
8. H. Kamano, S. X. Nakamura, T.-S. H. Lee and T. Sato, *Phys. Rev. C* **90**, no. 6, 065204 (2014).
9. H. Kamano, S. X. Nakamura, T.-S. H. Lee and T. Sato, *Phys. Rev. C* **92**, no. 2, 025205 (2015) Erratum: [*Phys. Rev. C* **95**, no. 4, 049903 (2017)].
10. H. Kamano and T.-S. H. Lee, *Phys. Rev. C* **94**, no. 6, 065205 (2016).
11. C. Fernandez-Ramirez, I. V. Danilkin, D. M. Manley, V. Mathieu and A. P. Szczepaniak, *Phys. Rev. D* **93**, no. 3, 034029 (2016).
12. K.H. Hicks and H. Sako, “P45: 3-Body Hadronic Reactions for New Aspects of Baryon Spectroscopy”, Proposal for J-PARC E45 (2013).
13. S. Adhikari *et al.*, “Strange Hadron Spectroscopy with a Secondary K_L Beam at GlueX”, Proposal for JLAB PAC45 (2017).
14. F. Iazzi [PANDA Collaboration], *AIP Conf. Proc.* **1743**, 050006 (2016).
15. M. T. Keil, G. Penner and U. Mosel, *Phys. Rev. C* **63**, 045202 (2001).
16. G. P. Gopal *et al.* [Rutherford-London Collaboration], *Nucl. Phys. B* **119**, 362 (1977).
17. A. Baldini, V. Flaminio, W. G. Moorhead, D. R. O. Morrison, in: *Landolt-Börnstein Band 12a*, Springer, Berlin 1988.
18. J. Gaiser [Crystal Ball Collaboration], SLAC Stanford - SLAC-PUB-2887 (82,REC.MAY) 15p.
19. J. K. Bienlein [Crystal Ball Collaboration], In *San Diego 1992, Photon photon collisions* 241-257.
20. B. M. K. Nefkens [Crystal Ball Collaboration], *Int. J. Mod. Phys. A* **20**, 1575 (2005)
21. R. Beck [Crystal Ball at MAMI and A2 Collaborations], *Prog. Part. Nucl. Phys.* **55**, 91 (2005).
22. A. Starostin *et al.* [Crystal Ball Collaboration], *Phys. Rev. C* **64**, 055205 (2001).
23. S. Prakhov *et al.*, *Phys. Rev. C* **80**, 025204 (2009).
24. R. Manweiler *et al.*, *Phys. Rev. C* **77**, 015205 (2008).
25. S. Prakhov *et al.* [Crystal Ball Collaboration], *Phys. Rev. C* **69**, 042202 (2004).
26. S. Prakhov *et al.* [Crystal Ball Collaboration], *Phys. Rev. C* **70**, 034605 (2004).
27. K. Moriya *et al.* [CLAS Collaboration], *Phys. Rev. C* **87**, no. 3, 035206 (2013)
28. K. Moriya *et al.* [CLAS Collaboration], *Phys. Rev. C* **88**, 045201 (2013).
29. K. Moriya *et al.* [CLAS Collaboration], *Phys. Rev. Lett.* **112**, no. 8, 082004 (2014).
30. A.V. Sarantsev, M. Matveev, V.A. Nikonov, A.V. Anisovich, U. Thoma, and E. Klempt, “Hyperon II: Properties of excited hyperons”, accompanying paper.
31. U. Löring, B. C. Metsch and H. R. Petry, *Eur. Phys. J. A* **10**, 447 (2001).
32. A.V. Anisovich, A.V. Sarantsev, V.A. Nikonov, V. Burkert, R. Schumacher, and E. Klempt, “Hyperon III: Study of $\Lambda(1405)$ ”, in preparation.
33. D. N. Tovee *et al.*, *Nucl. Phys. B* **33**, 493 (1971).
34. R. J. Nowak *et al.*, *Nucl. Phys. B* **139**, 61 (1978).
35. M. Bazzi *et al.* [SIDDHARTA Collaboration], *Phys. Lett. B* **704**, 113 (2011).
36. M. Bazzi *et al.*, *Nucl. Phys. A* **881**, 88 (2012).
37. J. A. Oller and U. G. Meißner, *Phys. Lett. B* **500**, 263 (2001).
38. E. Oset, A. Ramos and C. Bennhold, *Phys. Lett. B* **527**, 99 (2002) Erratum: [*Phys. Lett. B* **530**, 260 (2002)].
39. D. Jido, J. A. Oller, E. Oset, A. Ramos and U. G. Meißner, *Nucl. Phys. A* **725**, 181 (2003).
40. A. Cieply and J. Smejkal, *Eur. Phys. J. A* **43**, 191 (2010).
41. Y. Ikeda, T. Hyodo and W. Weise, *Nucl. Phys. A* **881**, 98 (2012).
42. Z. H. Guo and J. A. Oller, *Phys. Rev. C* **87**, no. 3, 035202 (2013).
43. M. Mai and U. G. Meißner, *Nucl. Phys. A* **900**, 51 (2013).
44. M. Mai and U. G. Meißner, *Eur. Phys. J. A* **51**, 30 (2015).
45. L. Roca and E. Oset, *Phys. Rev. C* **87**, 055201 (2013).
46. L. Roca and E. Oset, *Phys. Rev. C* **88**, 055206 (2013).
47. A. Cieply, M. Mai, U. G. Meißner and J. Smejkal, *Nucl. Phys. A* **954**, 17 (2016).
48. K. Miyahara, T. Hyodo and W. Weise, *Phys. Rev. C* **98**, 025201 (2018).
49. A.V. Anisovich, V.A. Nikonov, A.V. Sarantsev, V. Burkert, R. Schumacher, U. Thoma, and E. Klempt, “Hyperon IV: Hyperon resonances from photoproduction”, in preparation.
50. B. Dey *et al.* [CLAS Collaboration], *Phys. Rev. C* **89**, no. 5, 055208 (2014).
51. A. Anisovich, E. Klempt, A. Sarantsev and U. Thoma, *Eur. Phys. J. A* **24**, 111 (2005) doi:10.1140/epja/i2004-10125-6 [hep-ph/0407211].
52. A. V. Anisovich and A. V. Sarantsev, *Eur. Phys. J. A* **30**, 427 (2006) doi:10.1140/epja/i2006-10102-1 [hep-ph/0605135].
53. A. V. Anisovich, V. A. Nikonov, A. V. Sarantsev, V. V. Anisovich, M. A. Matveev, T. O. Vulfs, K. V. Nikonov and J. Nyiri, *Phys. Rev. D* **84**, 076001 (2011). doi:10.1103/PhysRevD.84.076001
54. T. S. Mast, M. Alston-Garnjost, R. O. Bangerter, A. S. Barbaro-Galtieri, F. T. Solmitz and R. D. Tripp, *Phys. Rev. D* **14**, 13 (1976).
55. W. Cameron *et al.* [Rutherford-London Collaboration], *Nucl. Phys. B* **193**, 21 (1981).

56. B. Conforto *et al.* [Rutherford-London Collaboration], Nucl. Phys. B **105**, 189 (1976).
57. J. Griselin *et al.*, Nucl. Phys. B **93**, 189 (1975).
58. A. de Bellefon *et al.*, Nuovo Cim. A **42**, 403 (1977).
59. R. Armenteros *et al.*, Nucl. Phys. B **21**, 15 (1970).
60. C. J. Adams *et al.*, Nucl. Phys. B **96**, 54 (1975).
61. B. Conforto *et al.*, Nucl. Phys. B **34**, 41 (1971).
62. M. G. Albrow, S. Andersson-Almehed, B. Bosnjakovic, F. C. Erne, Y. Kimura, J. P. Lagnaux, J. C. Sens and F. Udo, Nucl. Phys. B **29**, 413 (1971).
63. C. Daum, F. C. Erne, J. P. Lagnaux, J. C. Sens, M. Steuer and F. Udo, Nucl. Phys. B **6**, 273 (1968).
64. S. Andersson-Almehed, C. Daum, F. C. Erne, J. P. Lagnaux, J. C. Sens and F. Udo, Nucl. Phys. B **21**, 515 (1970).
65. P. C. Barber *et al.*, Nucl. Phys. B **102**, 365 (1976).
66. P. C. Barber *et al.*, Nucl. Phys. B **92**, 391 (1975).
67. M. Jones, R. Levi Setti, D. Merrill and R. D. Tripp, Nucl. Phys. B **90**, 349 (1975).
68. P. J. Litchfield *et al.*, Nucl. Phys. B **30**, 125 (1971).
69. M. Alston-Garnjost, R. W. Kenney, D. L. Pollard, R. R. Ross, R. D. Tripp and H. Nicholson, Phys. Rev. D **17**, 2226 (1978).
70. R. Armenteros *et al.*, Nucl. Phys. B **8**, 233 (1968).
71. A. Berthon *et al.*, Nucl. Phys. B **20**, 476 (1970).
72. D. F. Baxter *et al.*, Nucl. Phys. B **67**, 125 (1973).
73. G. W. London *et al.*, Nucl. Phys. B **85**, 289 (1975).
74. A. de Bellefon *et al.*, Nuovo Cim. A **90**, 1 (1975).
75. A. Berthon *et al.*, Nucl. Phys. B **24**, 417 (1970).
76. A. de Bellefon *et al.*, Nuovo Cim. A **37**, 175 (1977).
77. M. D. Jones, Nucl. Phys. B **73**, 141 (1974).
78. J. P. Berge *et al.* Phys. Rev. **147**, 945 (1966).
79. G. Burgun *et al.* Nucl. Phys. B **8**, 447 (1968).
80. P. M. Dauber *et al.* Phys. Rev. **179**, 1262 (1969).
81. J. R. Carlson *et al.* Phys. Rev. D **7**, 2533 (1973).
82. A. de Bellefon *et al.*, Nuovo Cim. A **41**, 451 (1977).
83. T. G. Trippe *et al.* Phys. Rev. **158**, 1334 (1967).
84. W. P. Trower *et al.* Phys. Rev. **170**, 1207 (1968).
85. E. Briefel *et al.* Phys. Rev. D **16**, 2706 (1977).
86. A. J. Van Horn *et al.* Phys. Rev. D **6**, 1275 (1972).
87. R. A. Ponte *et al.* Phys. Rev. D **12**, 2597 (1975).
88. R. D. Ehrlich, B. Lovett, M. Mishina, P. A. Souder, J. Snyder, M. E. Zeller, D. M. Lazarus and I. Nakano, Phys. Lett. **71B**, 455 (1977).
89. H. C. Bryant *et al.*, Nucl. Phys. B **168**, 207 (1980).
90. D. A. Sharov, V. L. Korotkikh and D. E. Lanskoj, Eur. Phys. J. A **47**, 109 (2011).
91. A. Brandstetter *et al.*, Nucl. Phys. B **39**, 13 (1972).
92. A. Nakkasyan, Nucl. Phys. B **93**, 85 (1975).
93. B. Baccari *et al.*, Nuovo Cim. A **41**, 96 (1977).
94. P. J. Litchfield, R. J. Hemingway, P. Baillon, A. Putzer and H. Schleich, Nucl. Phys. B **74**, 19 (1974).
95. W. Cameron *et al.* [Rutherford-London Collaboration], Nucl. Phys. B **131**, 399 (1977).
96. W. Cameron *et al.* [Rutherford-London Collaboration], Nucl. Phys. B **143**, 189 (1978).
97. W. Cameron *et al.* [Rutherford-London Collaboration], Nucl. Phys. B **146**, 327 (1978).
98. P. J. Litchfield, R. J. Hemingway, P. Baillon, A. Albrecht and A. Putzer, Nucl. Phys. B **74**, 39 (1974).
99. J. Landay, M. Mai, M. Dring, H. Habertzettl and K. Nakayama, Phys. Rev. D **99**, no. 1, 016001 (2019).
100. A. V. Anisovich, E. Klempt, B. Krusche, V. A. Nikonov, A. V. Sarantsev, U. Thoma and D. Werthmiller, Eur. Phys. J. A **51**, no. 6, 72 (2015).
101. V. D. Burkert, R. De Vita, M. Battaglieri, M. Ripani and V. Mokeev, Phys. Rev. C **67**, 035204 (2003).
102. T. Boika, V. Kuznetsov and M. V. Polyakov, "The neutron anomaly in the $\gamma N \rightarrow \eta N$ cross section through the looking glass of the flavour SU(3) symmetry," unpublished note, arXiv:1411.4375 [nucl-th].
103. J. Olmsted *et al.* [Crystal Ball Collaboration], Phys. Lett. B **588**, 29 (2004).